The Site Tilt and Lander Transfer Function from the Short-Period Seismometer of InSight on Mars

Alexander Stott, Constantinos Charalambous, Tristram Warren, William Pike, Robert Myhill, Naomi Murdoch, John Mcclean, Ashitey Trebi-Ollennu, Grace Lim, Raphael Garcia, et al.

The site tilt and lander transfer function from the short period seismometer of InSight on Mars

Alexander E. Stott[1,2,*], **Constantinos Charalambous**[1], **Tristram J. Warren**[3], **William T. Pike**[1], **Robert Myhill**[4], **Naomi Murdoch**[2], **John B. McClean**[1,5], **Ashitey Trebi-Ollennu**[6], **Grace Lim**[6], **Raphael F. Garcia**[2], **David Mimoun**[2], **Sharon Kedar**[6], **Kenneth J. Hurst**[6], **Marco Bierwirth**[7], **Philippe Lognonné**[8,9], **Nicholas A. Teanby**[4], **Anna Horleston**[4] and **William B. Banerdt**[6]

[*] Corresponding author: Alexander E. Stott, alexander.stott@isae-supaero.fr

[1] Department of Electrical and Electronic Engineering, Imperial College London, London, UK

[2] Institut Supérieur de l'Aéronautique et de l'Espace SUPAERO, Toulouse, France

[3] University of Oxford, Department of Physics, Parks Road, Oxford OX1 3PU, UK

[4] School of Earth Sciences, University of Bristol, Bristol, UK

[5] MIT Haystack Observatory, 99 Millstone Rd, Westford, MA, 01886, United States

[6] Jet Propulsion Laboratory, California Institute of Technology, Pasadena, CA, USA

[7] Max Planck Institute for Solar System Research, Justus-von-Liebig-Weg 3, 37077 Göttingen, Germany

[8] Université de Paris, Institut de physique du globe de Paris, CNRS, Paris, France

[9] Institut Universitaire de France, 1 rue Descartes, Paris, France

Declaration of Competing Interests

The authors acknowledge there are no conflicts of interest recorded.

Abstract

The NASA InSight mission has deployed the seismic experiment, SEIS, on the surface of Mars and has recorded a variety of signals including marsquakes and dust devils. This work presents results on the tilt and local noise sources, which provide context to aid interpretation of the observed signals and allow an examination of the near surface properties. Our analysis uses data recorded by the short period (SP) sensors on the deck, throughout deployment and in the final configuration. We use thermal decorrelation to provide an estimate of the Sol to Sol tilt. This tilt is examined across deployment and over a Martian year. After each modification to the site, the tilt is seen to stabilise over 3–20 Sols depending on the action and the total change in tilt is $<$0.035 degrees. Long term tilt over a Martian year is limited to $<$0.007 degrees. We also investigate the attenuation of lander-induced vibrations between the lander and SEIS. Robotic arm motions provide a known lander source in the 5–9 Hz bandwidth, yielding an amplitude attenuation of lander signals between 100 and 1000 times. The attenuation of wind sensitivity, from the deck to ground, presents a similar value in the 1.5–9 Hz range, thus favouring a noise dominated by lander vibrations induced by the wind. Wind sensitivities outside this bandwidth exhibit different sensitivity changes, indicating a change in the coupling. The results are interpreted through a finite element analysis of the regolith with a depth-dependent Young's modulus. We argue that discrepancies between this model and the observations are due to local compaction beneath the lander legs and/or anelasticity. An estimate for the effective Young's modulus is obtained as 62–81 MPa, corroborating previous estimates for the top layer duricrust.

Introduction

The NASA InSight lander (Banerdt et al., 2020) has been operating for over a complete Martian year (approximately two Earth years). The seismic experiment, SEIS, includes two seismometers known as the short period (SP) microseismometer and the very broadband (VBB). As detailed in Lognonné et al. (2019), the VBB sensor has a self-noise floor of $\sim 3 \times 10^{-10}\,\mathrm{m/s^2/Hz^{1/2}}$ over the bandwidth 3×10^{-2}–7×10^{-1} Hz, whereas the SP sensor has a self-noise floor of $\sim 3 \times 10^{-9}\,\mathrm{m/s^2/Hz^{1/2}}$ over the bandwidth 0.1–7 Hz. Both the SP and VBB have been jointly recording throughout much of the mission to date (Ceylan et al., 2021; Clinton et al., 2021). The VBB sensor assembly, however, required levelling to within 0.1 degrees before operation and so

was initially inactive (Bierwirth et al., 2019). On the other hand, the SP is a MEMS (microelectromechanical system) sensor and is able to operate at a tilt of up to 15 degrees without recentering (Lognonné et al., 2019; Pike et al., 2016). As a result, the SP sensor began collecting data during the deployment phase between Sols 4 and 66, where a Sol is a Martian solar day with Sol 1 beginning the local mean solar time midnight after landing. This was before the VBB could operate. This includes 48 hours of data on the deck over seven Sols (between Sol 4 and 21) (Panning et al., 2020) and uncovered surface data from Sol 24 until SEIS reached its final setup on Sol 66 when the WTS (wind and thermal shield) was deployed (Lognonné et al., 2020). The SP sensor was even operated during cruise where it recorded its self-noise (McClean et al., 2019). This unique dataset was useful to make decisions during the deployment of SEIS and in Panning et al. (2020) has been used to assess the potential of future on-deck planetary deployments which could be a cost effective approach for some planetary seismic studies.

Prior to achieving its final installation, where the VBB sensor would continuously record in its high performance scientific mode in tandem with the SP, several further deployment activities were required to minimise the seismic noise from the lander and atmosphere of Mars and are detailed in Lognonné et al. (2019). These were:

- the tether storage box (TSB) release on Sol 37, to unveil the full tether length from its protective box after SEIS was deployed on the ground.
- three stages of levelling (LVL) on Sol 30, 39 and 44, where the legs of SEIS were expanded/contracted to move SEIS close to the ground and level.
- load shunt assembly (LSA) release on Sol 40. The LSA is the connection of the tether to SEIS and is designed to mechanically uncouple them, similarly to coiling cable around a seismometer.
- pinning mass adjustments on Sols 56, 59 and 61, where the tether was moved to open the LSA further.
- wind and thermal shield (WTS) deployment on Sol 66.

Several of these stages required the irreversible breaking of frangibolts that held the seismometer assembly in its stowed configuration. The levelling sequences consisted of extending/contracting

the three legs of the LVL system on which SEIS sits (Bierwirth et al., 2019; Lognonné et al., 2019). After each step, it was crucial to confirm that the current situation was stable and verify the site noise, tasks which the SP sensor could perform.

In this paper, we analyse the long period response of the seismometer to obtain a measurement of tilt and verify the stability of the site. To do this, we examine the SP mass position channel over the deployment and the science monitoring phases of the mission. The mass position channel is proportional to acceleration and is sometimes known as acceleration or tilt output of a seismometer. To compute the tilt, we first quantify the thermal response of the SP sensors (Stott et al., 2018a). This dominates the long period response of the sensor, particularly on a diurnal scale, and so must be removed before the tilt can be obtained. Two algorithms are proposed which remove the diurnal temperature response to give a relative, delta tilt between Martian Sols providing that the SP sensor remains within the same feedback null point. These null points are due to the operation of the sensor which is based on the force feedback principal of Wielandt et al. (1982). The sensor coils drive the proof mass to try to remain stationary at these null points. The SP implements a grid of several feedback null points in order to operate over a wide range of tilts (Lognonné et al., 2019; Pike et al., 2016). However, the SP temporarily loses feedback when transitioning between null points and the value of the mass position output may not physically correspond to that of the preceding null point. As such, the proposed methods only give the relative tilt between Sols while the sensor remains within a single null point. We do not examine tilts when the sensor transitions between them. These null points have a periodicity of $48\,\mu\mathrm{m}$, which means the feedback null transitions to another for a tilt of 1.58 degrees.

In this study, we analyse the extracted relative tilt on the deck, between each levelling operation on the ground and, after the final levelling operation, over the science monitoring phase of the mission. This provides an insight into the point stability (Kümpel et al., 2001) on Mars over nearly 2 Earth years.

The deployment data also provides important context for understanding local noise sources. The sensor is installed on the ground, shielded from direct wind forcing and the harsh Martian temperature variation by the WTS. However, wind can still force vibrations of the lander (with attached solar panels) and the WTS, which are coupled to SEIS through the martian regolith (Mimoun et al., 2017; Murdoch et al., 2018, 2017). Testing of the lander-ground interaction was not performed on

Earth prior to launch. While such testing would have provided useful information, it is not possible to replicate a suitable analogue of Martian conditions on Earth for a thorough examination (Panning et al., 2020). The data recorded on deck, however, provide an ability to quantify the atmospheric forcing on the lander and coupling through the Martian regolith.

InSight has a robotic arm known as the IDS (instrument deployment system) used for deploying and interacting with SEIS and other instruments (Trebi-Ollennu et al., 2018). Motions of the robotic arm produce vibrations which are experienced by the seismometer (Ceylan et al., 2021; Stott et al., 2020). Consider that the robotic arm motions observed by the seismometer on the deck can be compared to those observed on the ground to calculate the absolute part of the transfer function, a transfer coefficient, in the 5–9 Hz bandwidth. This follows a preliminary investigation into the robotic arm motions in (Stott et al., 2020). The observed transfer coefficient for this lander-induced signal is then compared with the wind-induced acceleration over a range of frequencies. In doing so, we highlight the lander as a source of vibrations. Moreover, we observe the seismometer's sensitivity to wind without added cultural noise that would be seen on Earth.

To understand the factors at play for these attenuation estimates, we present a finite element model (FEM) which simulates the elastic deformation of the Martian regolith resulting from vibrations of the lander feet building upon the pre-launch studies of Teanby et al. (2017) and Myhill et al. (2018). This simulation models the regolith as an elastic half-space with a depth-dependent Young's modulus. In addition, we estimate the effective Young's modulus through a consideration of the equation of motion for the lander with the wind forcing and the SP acceleration on the lander.

SEIS site stability from tilt

SP long period response and temperature sensitivity

The long period response of horizontal seismometers can be inferred to be due to tilting (De Angelis et al., 2012; Rodgers, 1968) and so we must retrieve the low frequency acceleration from the SP. As detailed in Stott et al. (2018a), the SP has two outputs from the force feedback system: the velocity and mass position channel. These two channels are the outputs of the two coils used to drive the sensor feedback. The velocity channel is the main scientific output digitised at 24 bits for fine control whereas the mass position is used for coarser control of large displacements and is

digitised at 12 bits. The velocity channel is proportional to the velocity above the sensor transfer function corner frequency $\sim 1/35$ Hz and the mass position output is proportional to acceleration at frequencies below this corner frequency. To this end, the SP sensor mass position output can be used to retrieve the acceleration at long periods through multiplying the signal by a gain. Further technical specification and details on the SP transfer function can be found in Lognonné et al. (2019) and Stott et al. (2018a).

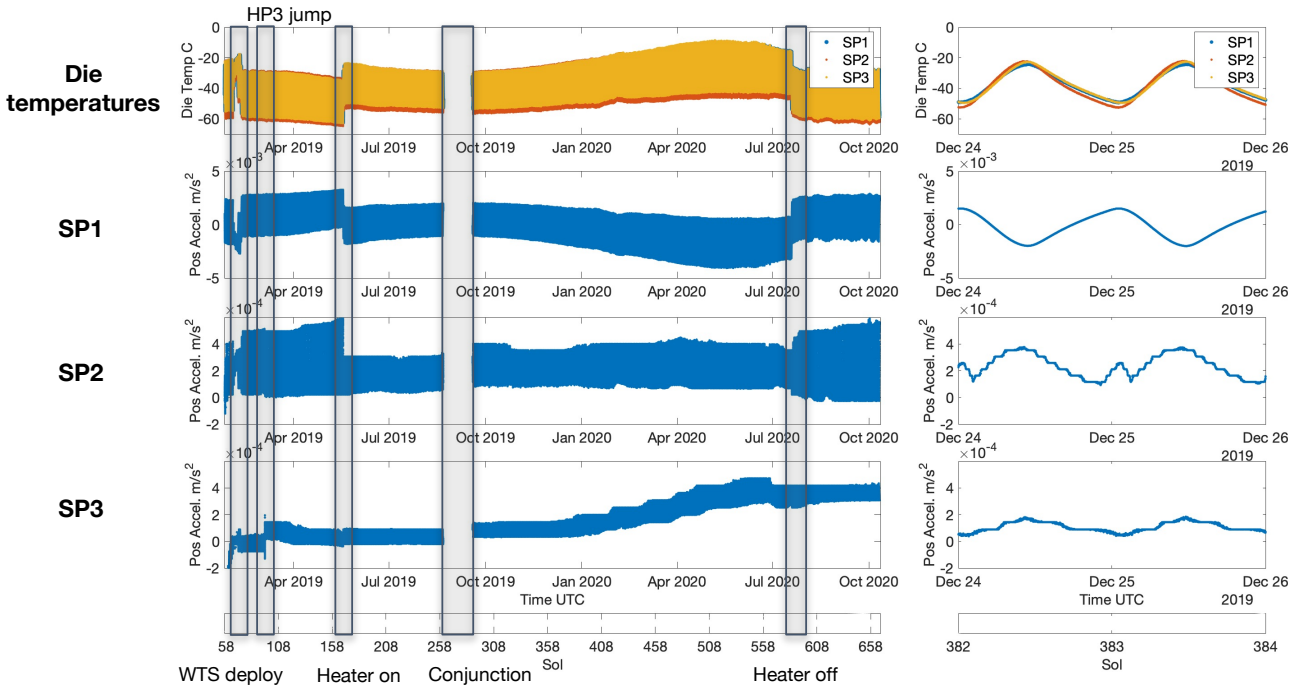

Figure 1. The sensors die temperature (top row) and mass position of the SP1 (vertical, second row), SP2 (horizontal, third row) and SP3 (horizontal, fourth row) sensors from Sol 58 to Sol 668. Several key events in Table 1 are indicated. Note that the vertical variation in the mass position is the diurnal variation, highlighted in the second column which shows a zoom over 2 Sols. For SP1 and SP2 this is the most significant motion over the Martian year but for SP3 the annual variation is of an equivalent magnitude.

Figure 1 shows the acceleration from SP mass position channels for each sensor from Sol 58 to Sol 667 along with their die temperatures. Note that there is a large data gap during solar conjunction, when Mars passed around the opposite side of the Sun, prohibiting direct communication. Just prior to this, the SEIS system fell into safe mode and so could not record during this period. This could not be restored until communication with the spacecraft was re-established. The key

Event	Sol
Landing	Sol 0
First SP data	Sol 4
SEIS deployed on the ground	Sol 22
Levelling motions	Sol 30, 39 and 44
Tether storage box (TSB) release	Sol 37
Load shunt assembly (LSA) release	Sol 40
Pinning mass adjustments	Sol 56, 59 and 61
WTS deployment	Sol 66
Mass position jump associated with HP3 hammering	Sol 95
Heater switch on/off	Sol 168 and 584
Conjunction data gap	Sol 261 to 288

Table 1: Summary of important events in the displayed data.

features observed in this time series are:

1. the WTS deployment on Sol 66.
2. a jump in the mass position on Sol 95 associated with the second sequence of HP3 hammering, most notable in SP3.
3. the heater switch on (used to keep the sensors within the operating conditions) on Sol 168.
4. a large gap from Sol 261 to 288 during conjunction.
5. the heater switch off on Sol 584.

A full list of significant events over the mission is given in Table 1. Aside from the mass position jump on Sol 95, each of these features was induced by a change in the thermal environment. As a result, before we consider a tilt derived from the SP sensors the temperature sensitivity must be addressed.

The middle row of Figure 2 shows the SP acceleration versus temperature for each sensor over the mission, including data on the deck and on the ground. Prior to launch, Stott et al. (2018a) derived a model to predict the SP acceleration from temperature effects as

$$a_{SP} = \alpha_{Die} T_{Die} + \alpha_{\Delta}(T_{Die} - T_{Enc}) \quad (1)$$

where a_{SP} is the acceleration (in $\mathrm{m/s^2}$) of the SP, T_{Die} is the SP sensor die temperature (in C) and T_{Enc} is the temperature (in C) of the SP enclosure. This model takes into account two physical pathways, the change in Young's modulus with temperature of the sensor's cantilever (the sensor spring) and a thermoelastic component due to a temperature difference between the sensor and its enclosure. Stott et al. (2018a) found these two pathways to be sufficient to model the SP's acceleration output in pre-mission testing and depend on the instantaneous sensor (die) and enclosure temperature. The α_{Die} coefficient accounts for the change in the cantilever's Young's modulus with temperature while the α_{Δ} coefficient accounts for a thermoelastic effect from the temperature difference to SP enclosure (Liu et al., 2019; Stott et al., 2018a). The thermal model (1) can be written as a regression format as

$$\mathbf{y} = \mathbf{X}\mathbf{b}$$

where N data samples $1, 2, \ldots, N$ are collated into the vectors/matrices as

$$\mathbf{y} = [a_{1,2,\ldots,N}], \qquad \mathbf{X} = \left[T_{Die,1,2,\ldots,N}, \quad (T_{Die,1,2,\ldots,N} - T_{Enc,1,2,\ldots,N}), \quad 1_{1,2,\ldots,N}\right], \qquad (2)$$
$$\mathbf{b} = \left[\alpha_{Die}, \quad \alpha_{\Delta}, \quad \alpha_{DC}\right]^{\mathsf{T}},$$

The parameters α_{Die} and α_{Δ} are calculated through the least squares solution $\mathbf{b} = (\mathbf{X}^{\mathsf{T}}\mathbf{X})^{-1}\mathbf{X}^{\mathsf{T}}\mathbf{y}\prime$ where $\mathbf{y}\prime$ refers to a vector of measured SP acceleration values rather than an estimate of them.

The model parameters were fitted to mission data, shown in Figure 2. The on-deck response of the horizontal sensors changes from deck to ground while the vertical SP1 sensor has similar sensitivity for both datasets. The horizontal response on the deck, however, could not be well fitted by the thermal model (1). This indicates an additional thermoelastic contribution from the lander. We now consider the temperature sensitivities seen on the ground. The observed responses are not exactly the same as those from the pre-launch testing. These exhibited a strong thermoelastic, α_{Δ}, contribution for both the vertical and horizontal sensors. On Mars, however, the acceleration of the vertical SP1 sensor can be explained by a linear sensitivity to the die temperature fitted as $\alpha_{Die} = -1.4 \times 10^{-4}\,\mathrm{m/s^2/K}$ using (2). The horizontal SP2 sensor shows a piecewise linear sensitivity, which is also demonstrated in the time series in Figure 1. As this is a horizontal sensor it is sensitive to thermoelastic tilting. This bilinear sensitivity could then be due to a change in contact points of the sensor mounting, whereby a gap may open and close at a certain threshold. This would alter the thermoelastic forces on the sensor and therefore, the sensitivity to temperature.

Below -49C the thermal model was fitted to SP2 as $\alpha_{Die} = -4.2 \times 10^{-5}\,\mathrm{m/s^2/K}$ and above -49C by $\alpha_{Die} = 8.9 \times 10^{-6}\,\mathrm{m/s^2/K}$ and $\alpha_{\Delta} = -6.7 \times 10^{-5}\,\mathrm{m/s^2/K}$. The other horizontal SP3 was fitted by just the linear component as $\alpha_{Die} = 8.1 \times 10^{-6}\,\mathrm{m/s^2/K}$.

Figure 2 shows the rtPSD (square root of the power spectral density) of each sensor's mass position channel after the solar conjunction data gap, the largest continuous trace. This is shown alongside the fitted thermal model (the estimate $\mathbf{y} = \mathbf{Xb}$ from (2)) and a decorrelated response, whereby the estimate $\mathbf{y} = \mathbf{Xb}$ was subtracted from the mass position data.

For the vertical SP1, the decorrelation reduces both the diurnal peak, its harmonics and the long period response. At frequencies above $5 \times 10^{-5}\,\mathrm{Hz}$ (higher than the diurnal variation) the decorrelated signal has a generally higher power than the acceleration. This is because the temperature sensor has too high a noise above these frequencies to decorrelate successfully. Although the diurnal harmonics are still reduced, the noise floor is increased above what would be the sensor noise floor. This effect is only observed for the vertical SP1 data. The decorrelation for the horizontal sensors similarly suppresses diurnal peaks. The long period decorrelation has removed less power in comparison to the vertical. This is because they generally have a lower sensitivity to temperature, for example, SP3 shows a long term trend which is not well correlated with the die temperature. For some higher frequency harmonics, the decorrelation has not removed all the variation. This could be due to the low resolution of the data, as these channels are recorded as housekeeping data and so are digitised over 12 bits which limits the resolution (Lognonné et al., 2019). While this is important to consider these aspects with respect to the SP noise floor and temperature induced noise the decorrelation is sufficient for the scope of this paper. This is because our approaches focus on separating the thermal response from the DC component over the diurnal scale. From Figure 2, the average attenuation in amplitude at the diurnal peak is by a factor of 62, 8 and 3 for SP1, SP2 and SP3 respectively.

Obtaining the relative tilt from the SP horizontal sensors

After accounting for diurnal variation due to temperature in the SP acceleration, the long period acceleration of the horizontal sensors can be attributed to changes in tilt. We propose two methods to estimate this acceleration:

1. obtain the mass position values for SP2 and SP3 at a reference temperature each Sol.

2. calculate the thermal model response for SP2 and SP3 for each Sol and compare the DC bias component.

These approaches are summarised as algorithms in Tables 2 and 3 respectively and remove the temperature sensitivity for each Sol. Note that the output tilt values $\theta_{SP2,n}$ and $\theta_{SP3,n}$ therefore require a calibration in order to equate to an absolute tilt of the SEIS assembly. The subtraction of the acceleration of the first Sol in the sequence as $a_{SP2,n} = a_{SP2,n} - a_{SP2,1}$ and $a_{SP3,n} = a_{SP3,n} - a_{SP3,1}$ means that the output tilt is a relative, delta tilt.

Algorithm 1: Constant temperature based tilt algorithm

1: **Input:** T_{ref}**,** $T_{DIE,SP2}$**,** $T_{DIE,SP3}$**,** a_{SP2}**,** a_{SP3}**,** $g = 3.711m/s^2$
2: **for** Each Sol in sequence $n = 1, 2, \ldots, N$ **do**
3: Find the value $a_{SP2,n} = a_{SP2}(T_{DIE,SP2} = T_{ref})$ when $T_{DIE,SP2}$ is falling
4: Find the value $a_{SP3,n} = a_{SP3}(T_{DIE,SP2} = T_{ref})$ when $T_{DIE,SP2}$ is falling
5: Subtract the value of the first Sol in the sequence $a_{SP2,n} = a_{SP2,n} - a_{SP2,1}$ and $a_{SP3,n} = a_{SP3,n} - a_{SP3,1}$
6: $\theta_{SP2,n} = \arcsin a_{(SP2,n}/g)$
7: $\theta_{SP3,n} = \arcsin a_{(SP3,n}/g)$
8: Store $\theta_{SP2,n}$ and $\theta_{SP3,n}$
9: **end for**

Table 2: A tilt retrieval algorithm based on taking the acceleration values when the sensor is at a reference temperature.

The relative tilt over the deployment phase

The two tilt algorithms in Tables 2 and 3 were applied to the deployment data, beginning on the deck and then on the ground until SEIS was covered by the WTS. We separated the estimates of relative tilt over the deployment into five sections:

1. On the deck - Sol 10 to 21 (the first recording on Sol 4 was for only 10 minutes),

2. First placed on the ground - Sol 23 to 30,

Algorithm 2: Thermal decorrelation based tilt algorithm

Input: $T_{DIE,SP2}$, $T_{DIE,SP3}$, a_{SP2}, a_{SP3}, $g = 3.711m/s^2$
for Each Sol in sequence $n = 1, 2, \ldots, N$ **do**
    Calculate least squares regression to fit thermal model for $a_{SP2}(T_{DIE,SP2} > -49C)$
    Calculate least squares regression to fit thermal model for a_{SP3}
    Take the DC bias of each regression as $a_{SP2,n} = a_{DC,SP2}$ and $a_{SP3,n} = a_{DC,SP2}$
    Subtract the value of the first Sol in the sequence $a_{SP2,n} = a_{SP2,n} - a_{SP2,1}$ and $a_{SP3,n} = a_{SP3,n} - a_{SP3,1}$
    $\theta_{SP2,n} = \arcsin\left(a_{SP2,n}/g\right)$
    $\theta_{SP3,n} = \arcsin\left(a_{SP3,n}/g\right)$
    Store $\theta_{SP2,n}$ and $\theta_{SP3,n}$
end for

Table 3: A tilt retrieval algorithm based on taking the bias obtained from the thermal model decorrelation.

3. After the first levelling motion - Sol 31 to 39,

4. After the second levelling "MEMS offset tuning" motion - Sol 40 to 44,

5. After the third levelling low motion - Sol 45 onward.

Each section is separated by an action causing a change in the feedback null point, either the sensor being moved or a levelling motions. In a levelling activity, the legs of the LVL (that SEIS is mounted on) are actuated in order to get the SEIS assembly close to the ground and level (Bierwirth et al., 2019). During these motions, the horizontal SP sensors moved through feedback null points (which occur at tilt intervals of 1.58 degrees) and the mass position channel output was at its maximum slew rate (Lognonné et al., 2019). Over a null point transition, the mass position outputs are not physically comparable and so the proposed tilt algorithms cannot be used to estimate the tilt through, or compare before and after, these levelling motions. The tilt estimate for each Sol is, therefore, the relative tilt referred to the first Sol of its section. Before the WTS was deployed the SP was switched off overnight on each Sol as the sensor was outside the thermal limits for

239 operation, meaning that the sensor was not continuously in feedback. During this phase we assume
240 that the SPs remained within the same feedback null point when turned back on.

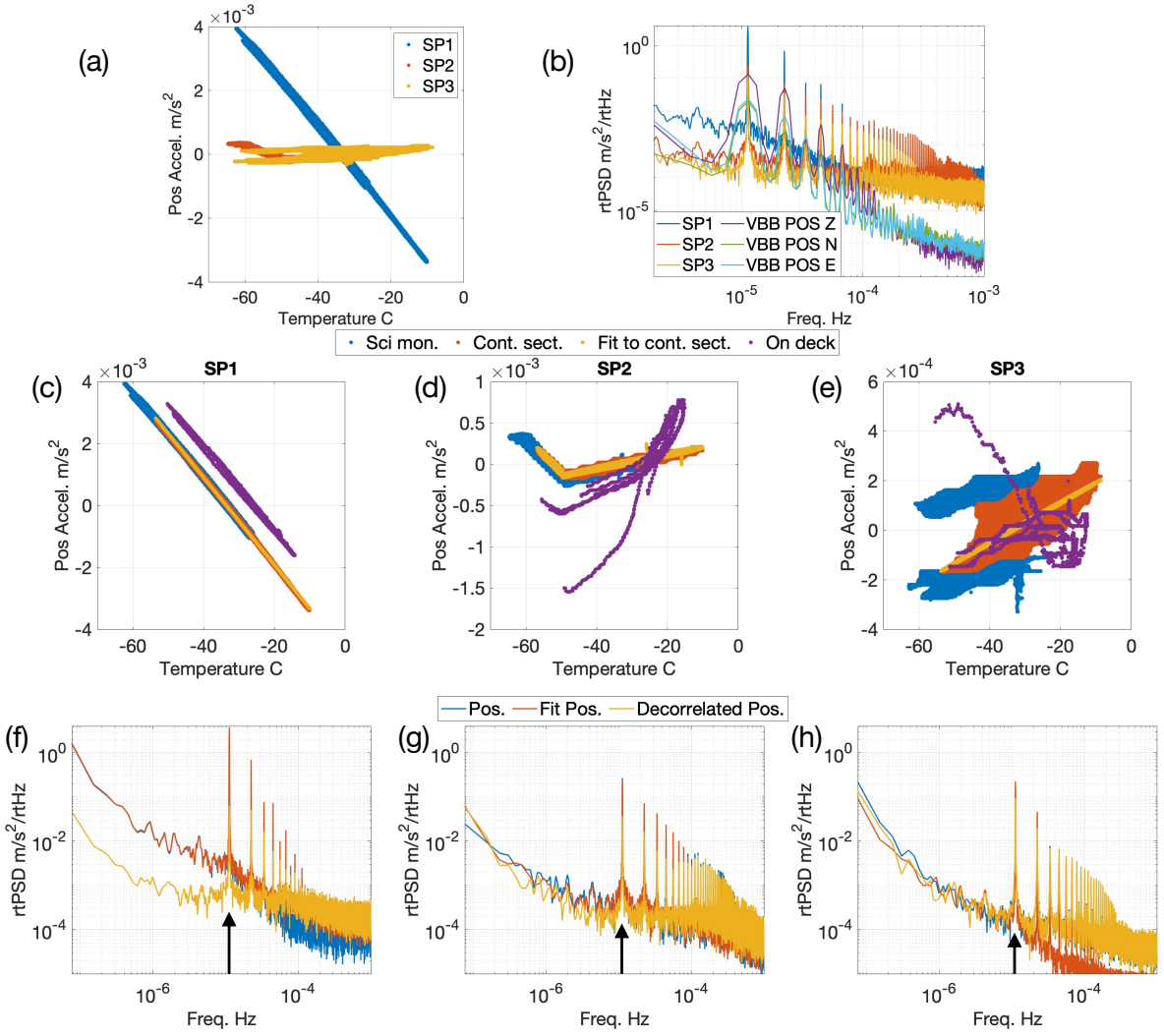

Figure 2. (a): The temperature versus acceleration (from mass position output) for SP1, SP2 and SP3 all together to show the relative differences. (b): The SP and VBB mass position rtPSDs showing the relative level of noise. (c), (d) and (e): the temperature versus acceleration (from mass position output) separately for SP1, SP2 and SP3. The blue data are for after the WTS from Sol 73 to 667, the red data correspond to the period after the solar conjunction to the heater turn off on Sol 584 which is the longest continuous section under the same thermal environment, the yellow are the output of the fitted thermal model to this longest continuous section and the purple are the SP response from on the deck. In each case the data are set to have zero mean. (f), (g) and (h): the rtPSD of SP1, SP2 and SP3 respectively for the longest continuous section (blue), the fitted thermal model output (red) and the decorrelated (the thermal model is subtracted from the original data) data (yellow). The arrow indicates a period of a Martian Sol.

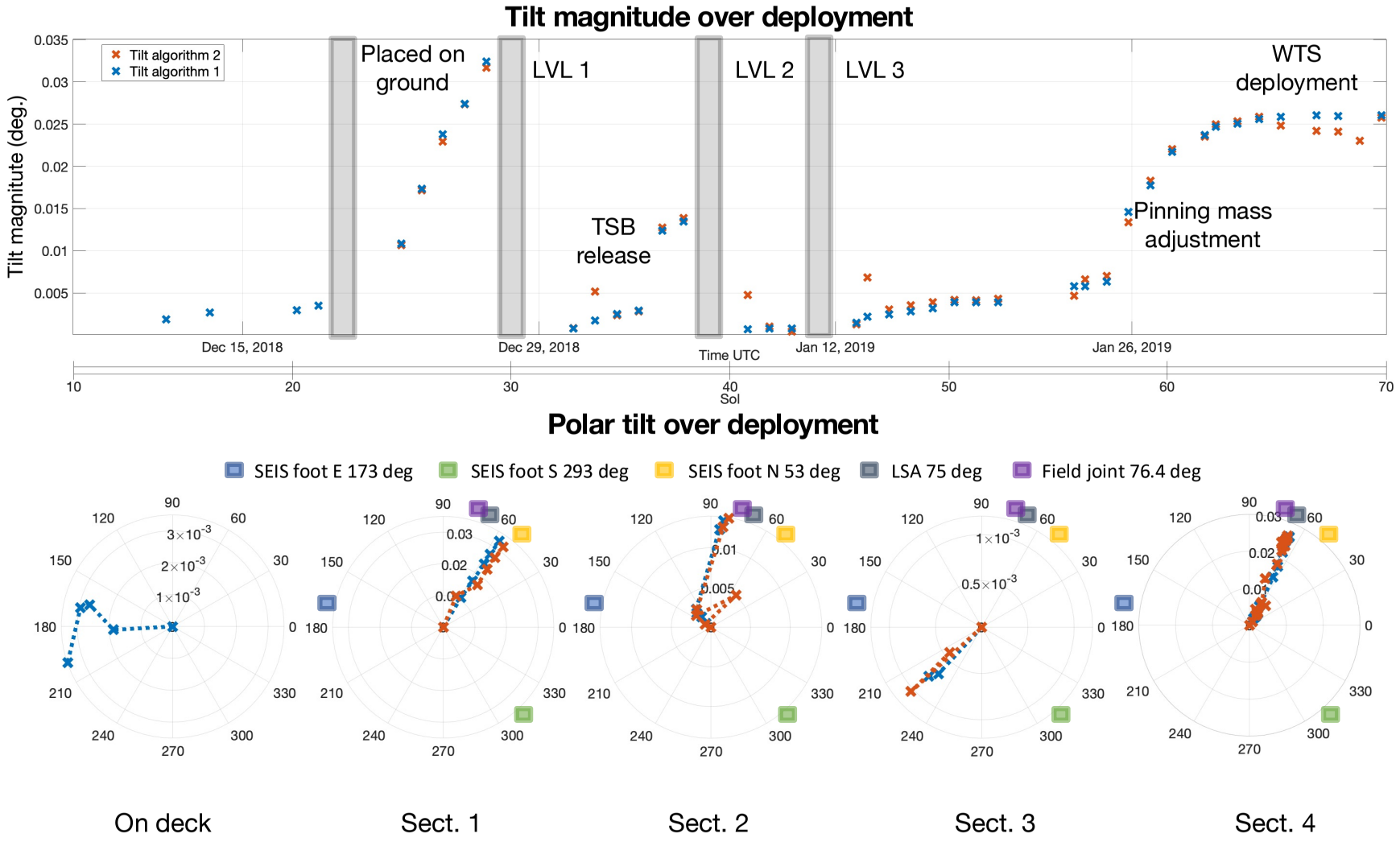

Figure 3. The evolution of tilt over the deployment phase of the mission until Sol 70. The top row shows the aggregate delta tilt for each data section beginning on the deck, separated by deployment/levelling activities (indicated by the grey boxes) which prevent the SP staying in feedback so tilt cannot be calculated between the before and after. The bottom row gives the polar plot of these tilts with the direction of key features indicated.

Figure 3 shows the tilt, in magnitude and direction, relative to the first Sol of each of the five sections calculated with both algorithms in Tables 2 and 3, and rotated into geographic coordinates where east is at 0 degrees azimuth and north at 90 degrees azimuth. The location of each item around SEIS is detailed in Ceylan et al. (2021) and Lognonné et al. (2019). A constant reference SP2 temperature of $T_{ref} = -25\,\mathrm{C}$ was used for the reference temperature based algorithm in Table 2. It can be seen that the two tilt retrieval algorithms in Tables 2 and 3 are in general agreement. The tilt derived from the thermal decorrelation based algorithm in Table 3 sometimes produces erroneous values owing to a poor fit of the thermal model on that Sol, e.g. in the third section on the ground an erroneous value was observed when the LSA was opened or in the final section after the WTS was deployed. Only tilt estimates from the reference temperature algorithm in Table 2 are presented for the on deck section. This is because the relationship between the horizontal SPs (SP2 and SP3) and their die temperature for the on deck section of data (shown in Figure 2) is not modelled by (1) and so the thermal decorrelation based algorithm in Table 3 cannot be used to retrieve a tilt estimate. This different relationship for the horizontal SPs on the deck and on the ground could be due to extra thermoelastic contributions from the assembly being bolted to the deck.

During the 11 Sols since the first long term SP acquisition on the deck on Sol 10, the cumulative tilt did not exceed 0.005 degrees, generally tilting toward the west but with a varying azimuth. This shows that the lander was reasonably stable at this point. The largest rate of tilting was observed during the first 7 Sols on the ground, totalling 0.033 degrees at the end of that period. This happened at a slowly decreasing rate with an azimuth of $\sim$55 degrees, which is approximately in the direction of the SEIS north foot. The period after the first levelling sequence shows a much lower rate of tilt which again decreases over time with an azimuth of 140 degrees. On Sol 38 the TSB release was performed, marked by a large tilt with an azimuth of 80 degrees which is close to that of the tether field joint. The TSB release action was to unfurl the entire length of the tether to allow it to lie along the ground, uncoupling it from the lander. The third period on the ground is only a few Sols and shows very little tilt with an azimuth of 220 degrees. The final stage after the last levelling motion shows a period of settling where the assembly tilted up to 0.005 degrees and then a larger set of tilts associated with the pinning mass adjustments. The pinning mass is a mass with a hook attached so that the robotic arm can move it to widen the gap of the LSA and

in turn help uncouple the tether from the SEIS assembly. After these motions, the tilt stabilised at 0.026 degrees for the WTS deployment. This tilt had an azimuth of 65 degrees which is between the LSA/field joint and the SEIS north foot.

The relative tilt over the science monitoring phase

The final stage of deployment was the emplacement of the WTS. Once the thermal environment had stabilised, the SP and VBB were placed in continuous operation for the science monitoring phase. The tilt algorithms in Tables 2 and 3 were applied to this continuous phase, with the reference Sol corresponding to the end of the final levelling sequence on Sol 44. Figure 4 shows the results in terms of the aggregate tilt and azimuth which demonstrate that the cumulative tilt of the SEIS assembly is $<$0.007 degrees since Sol 70 and is therefore extremely stable. A jump in the tilt is observed early in the mission on Sol 95 (March 2019) associated with the HP3 hammering and is seen in the mass position data in Figure 1, most notably on SP3. There is a broad agreement between the two algorithms with a generally constant difference of around 0.003 degrees. The constant SP2 temperature, T_{ref}, used for the algorithm in Table 2 was changed to $-35\,\mathrm{C}$ compared to the $-25\,\mathrm{C}$ used to analyse deployment. The change in reference temperature is because data was not recorded at the same reference temperature (on the rising edge) on all Sols as the sensor was turned off overnight. This does not affect the comparison of the results between sections as the temperature is a reference point to compare Sol to Sol acceleration values.

A very gradual apparent tilting can be observed during the scientific monitoring phase (Figure 4) whose rate increases slightly after Jan 2020. Additionally, there appears to be a three-month (Earth) quasiperiodic tilt signal with a peak to peak amplitude of 0.002 degrees. This is most notable in the thermal decorrelation based algorithm in Table 3 between Sol 94 and 244. Figure 5 shows the tilt since Sol 44 in Cartesian coordinates. This shows that after the initial settling period in a direction between the LSA and north SEIS foot the long term tilt is not in a single direction.

Discussion of the tilt results

The derived tilt signals are estimates based on removing the diurnal temperature variation in the data and comparing the residual mean on a Sol to Sol basis. This means they do not account for unmodelled longer period temperature sensitivities. To this end, the estimates may encapsulate

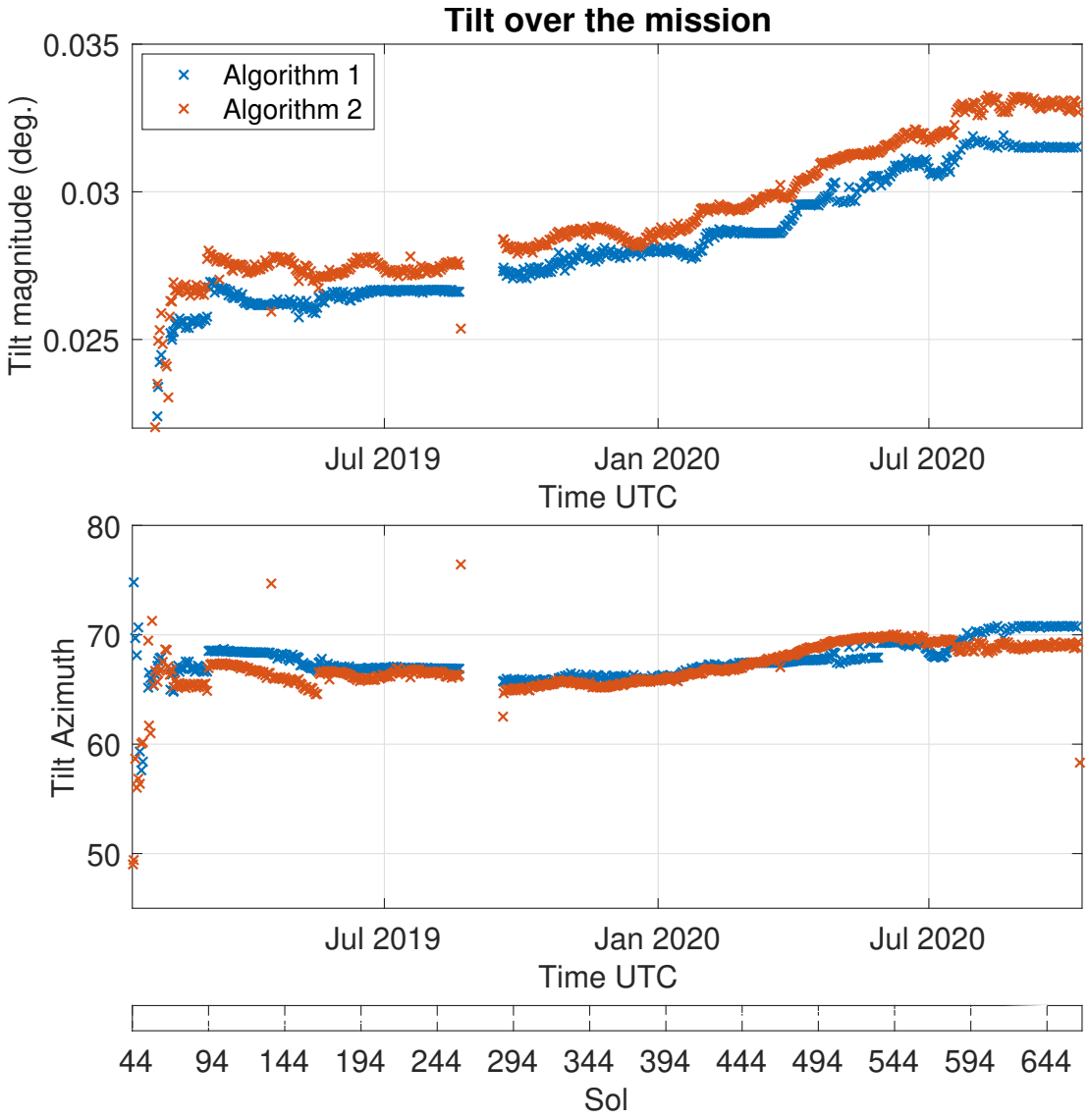

Figure 4. The evolution of tilt over the scientific monitoring phase of the mission from Sol 44 to 668. The tilt is the aggregate delta tilt referred to Sol 44, from where the SP has remained in the same feedback null. The blue data points correspond to the reference temperature based algorithm in Table 2 and the red data points to the thermal decorrelation based algorithm in Table 3.

both motion of the regolith and thermoelastic tilting of the SEIS assembly. On top of thermoelastic contributions from the SEIS assembly, the tilt estimates may also contain sensor drift. However, the aggregate tilt recorded since the beginning of the scientific monitoring phase is <0.007 degrees which corresponds to $4.5 \times 10^{-4}\,\mathrm{m/s^2}$. While we do not have a value for the sensor drift, it is above the sensor self-noise for this time period which is $\sim 5 \times 10^{-5}\,\mathrm{m/s^2/Hz^{1/2}}$ at $1 \times 10^{-8}\,\mathrm{Hz}$

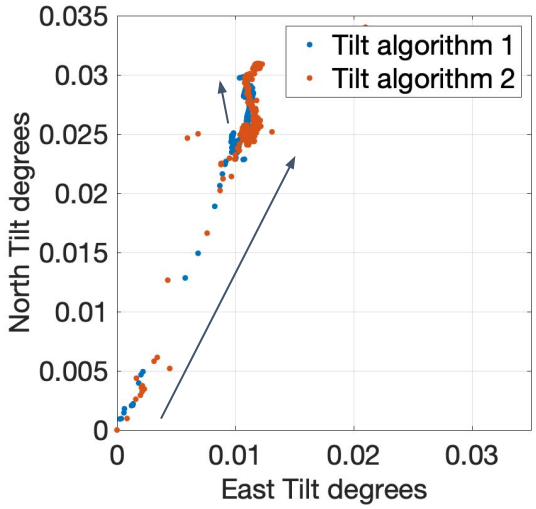

Figure 5. Tilt over the mission from Sol 44 to 668 in Cartesian coordinates, reported as the aggregate delta tilt. The blue data points correspond to the reference temperature based algorithm in Table 2 and the red data points to the thermal decorrelation based algorithm in Table 3. The direction of the tilting is indicated by the arrows. The largest arrow accounts for the tilt due to the pinning mass adjustments and initial settling. The tilt direction does fluctuate but generally progresses in the direction of the smaller arrow.

(Stott, 2018b).

There are several key features in the tilt estimates which do indicate a reasonable retrieval by the proposed algorithms. In the deployment phase, key activities resulted in an estimated tilt in the expected direction. For example, the response to the pinning mass adjustments shown in Figure 4. The long term overall settling (in Figure 4 and 5) after the final deployment step is towards the direction of the tether which could have been undergoing relaxation. The heater switch on/off significantly modified the thermal environment which could have induced a thermoelastic response in the SEIS assembly. The retrieved tilt signals show a small overall response to this large transient modification.

This work uses the SP sensor to examine the tilt as it was available to analyse the deployment phase of the mission, before the VBB could be used. Although the VBB has better low frequency performance than the SP sensor, the SP is suitable to look at the general tilt over the whole mission. The VBB requires occasional recentering and has active thermal compensation which is tuned every few months and so the long period data are interrupted and thermal response altered (Lognonné et al., 2019). This makes it difficult to establish a consistent tilt estimate over longer periods with the VBB. These tilt estimates derived from the SP can therefore be useful to aid future efforts to extract lower noise long period signals from the VBB. The VBB thermal noise and decorrelation are shown in supplement 1 of Lognonné et al. (2020). Figure 2 shows the rtPSDs of the acceleration derived from the VBB mass position output compared to the SP which indicates the level of thermal noise in each over such periods. The VBB has a lower sensitivity to temperature but it is still significant so that the thermal contribution must also be removed before a tilt can be extracted.

These algorithms are useful to examine the tilt in high noise environments, where the temperature is the dominant factor. Other factors such as pressure forcing (Ringler, 2020; Rodgers, 1968; Sorrells, 1971) could be considered to improve the model for other applications. If another such factor induced as significant a variation over a diurnal scale, the thermal model coefficients may be erroneous, affecting the decorrelation. The reference temperature based algorithm in Table 2, however, is not model based and so would not suffer from such an issue. As the tilt estimates from each algorithm agree, this indicates that the temperature is the dominant diurnal contribution, as expected in Mimoun et al. (2017).

The algorithms are also intended to be robust to issues with the data, for example, data gaps. During deployment the sensor was turned off over night and there are several smaller gaps throughout the mission. There are also several transient signals. As a result, an alternative, low-pass filter based approach to remove the diurnal variation would not be straightforward to implement for much of the data.

The main qualities of the tilt signal are the overall long period and the peak to peak variation. The long term aggregated tilt observed in the InSight data is <0.007 degrees and the largest peak to peak variation is the quasiperiodic three month variation which is limited to ~ 0.002 degrees. We can make a brief comparison to Earth studies to illustrate the various features of ground tilt estimates. Kümpel et al. (2001) found seasonal tilts in the north Rhine region have a peak to peak amplitude of

0.0046 degrees and the super-annual tilt of 0.0023 degrees per year. Petrosino et al. (2020) report a comparable super-annual tilt at the Campi Flegrei caldera. These studies highlight that seasonal effects on Earth are driven by tidal stresses and temperature. These factors are influenced strongly by the water cycle which generates changes in the ground medium and particularly impacts near surface deployments (Wolin et al., 2015) which would be absent at InSight (Golombek et al., 2017). As we only have one Martian year of data, the seasonal effects cannot be fully separated from super-annual tilt. Further data collection over several Martian years would help identify any seasonal change or periodicity.

The effect of lander-induced vibrations

Robotic arm motions as a source of lander motion

The signature of robotic arm motions in the seismic data

In order to deploy the SEIS assembly on the surface of Mars, the InSight lander is equipped with a robotic arm known as the Instrument Deployment Arm (IDA) (Trebi-Ollennu et al., 2018). This robotic arm also has a camera which is used for deployment and scientific imaging (Maki et al., 2018). During an arm motion, vibrations are also sensed in the SEIS data. The signature of such motions (Ceylan et al., 2021; Stott et al., 2020) in the spectrogram consist of:

1. broadband excitation above $4\,\mathrm{Hz}$
2. excitation of narrowband modes
3. excitation of several chirp signatures

A set of spectrograms of seismic records of lander motions are shown in Figure 6 which exhibit these characteristics. On the deck, the amplitude is larger but detail is often obscured by higher environmental noise. The two most significant chirping signatures, a tone changing in frequency over time, have frequencies of 4–$9\,\mathrm{Hz}$ and 10–$20\,\mathrm{Hz}$. The arm motions are typically between a few seconds to a few minutes long. The chirping depends on the arm motor positions. Timings of arm activity are used by the marsquake service to confirm they do not overlap with a detected marsquake (Ceylan et al., 2021; Clinton et al., 2021).

Using robotic arm motions to estimate the attenuation of lander motions

These robotic arm motions provide a known source of vibrations and were observed by the SP sensors both on and off the deck. We compare the recorded signatures on and off the deck and estimate the ratio of the robot arm excited amplitudes. This is the absolute part of the transfer function for a lander-induced vibration through the lander legs and regolith to SEIS, and thus provide a calibration for lander-induced noise sources. The absolute part of this transfer function is termed the transfer coefficient. This builds upon an experiment performed in Iceland by Teanby et al. (2017), where a wind driven mass on a spring system was used to simulate forcing from the WTS by wind. This work and a follow up study from Myhill et al. (2018) showed that in situ estimations of this transfer coefficient are required to update noise injection models and therefore to understand the site noise.

In order to achieve this, we must identify two similar arm motions performed on and off the deck. A candidate motion is the "Tau sequence" which directs the camera towards the sky to measure the optical depth of the atmosphere (Banfield et al., 2020; Maki et al., 2018). Similar motions were performed on Sol 14 on the deck and on Sol 71 on the ground covered by the WTS in the final observational configuration (Stott et al., 2020). These are shown in Figure 7 along with the arm joint positions. The arm elbow position correlates to the lower frequency chirp 4–$9\,\mathrm{Hz}$ across both of these motions, indicating it is the driver of this motion. This is confirmed as the arm position can be used to predict the frequency of the chirp through multiplying the square of the position by a constant factor of 0.6 and adding a bias of $3.8\,\mathrm{Hz}$ across motions, as shown in Figure 7 where the scaled elbow position is superimposed on the spectrogram chirp. This chirp is a good candidate signal for which to measure the attenuation as it has a relatively high SNR both on and off the deck and can be separated from lander mode excitation from other sources. Furthermore, the chirp signature only occurs while the robot arm is moving (as seen by the match to the elbow motor position) and is not excited by the ambient wind.

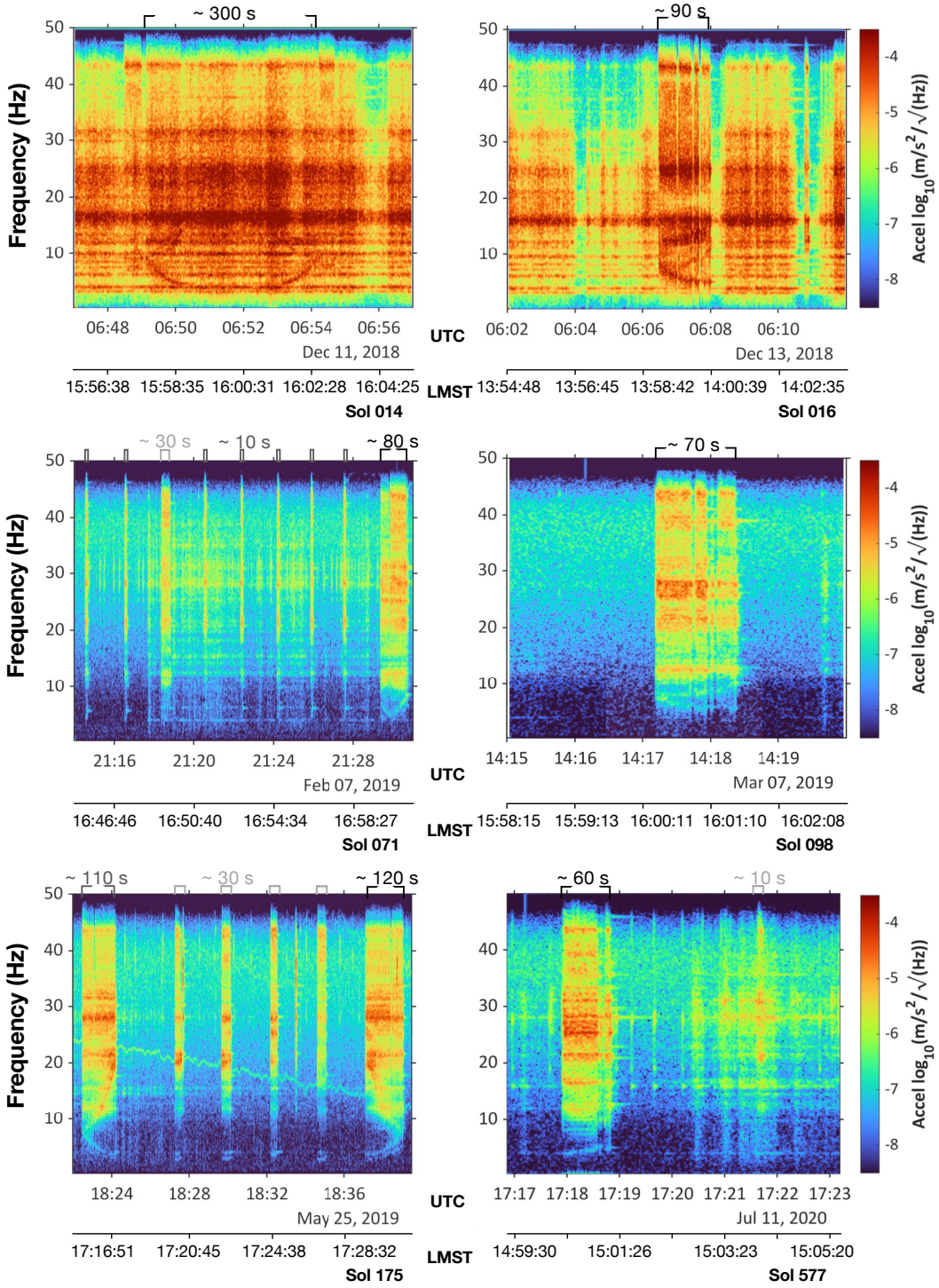

Figure 6. Spectrograms of 100 sps SP vertical (Z) data illustrating robot arm example signatures over the mission. For Sols 14 & 16 SEIS was uncovered on deck, while for Sols 71, 98, 175 & 577 SEIS was covered by the WTS on the ground. The duration of the robotic arm motions are indicated at the top.

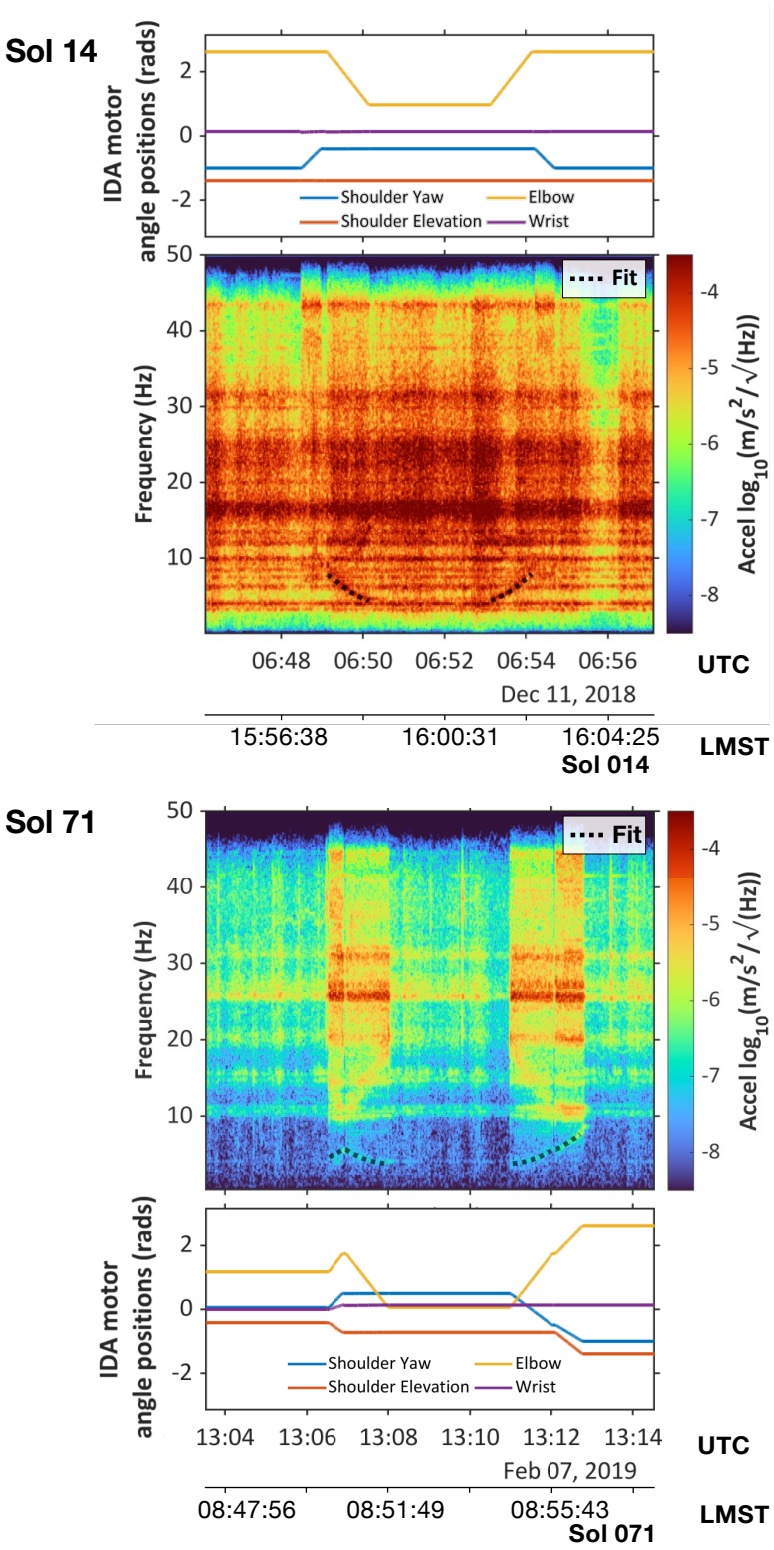

Figure 7. The spectrogram of the SP vertical (Z) acceleration and corresponding robot arm motor positions for the Tau estimation poses on Sol 14, SEIS on the deck, and Sol 71, SEIS on the ground, respectively. The overlayed fit, black dotted line, is the square of the elbow motor position scaled by 0.6 with a 3.8 Hz bias added.

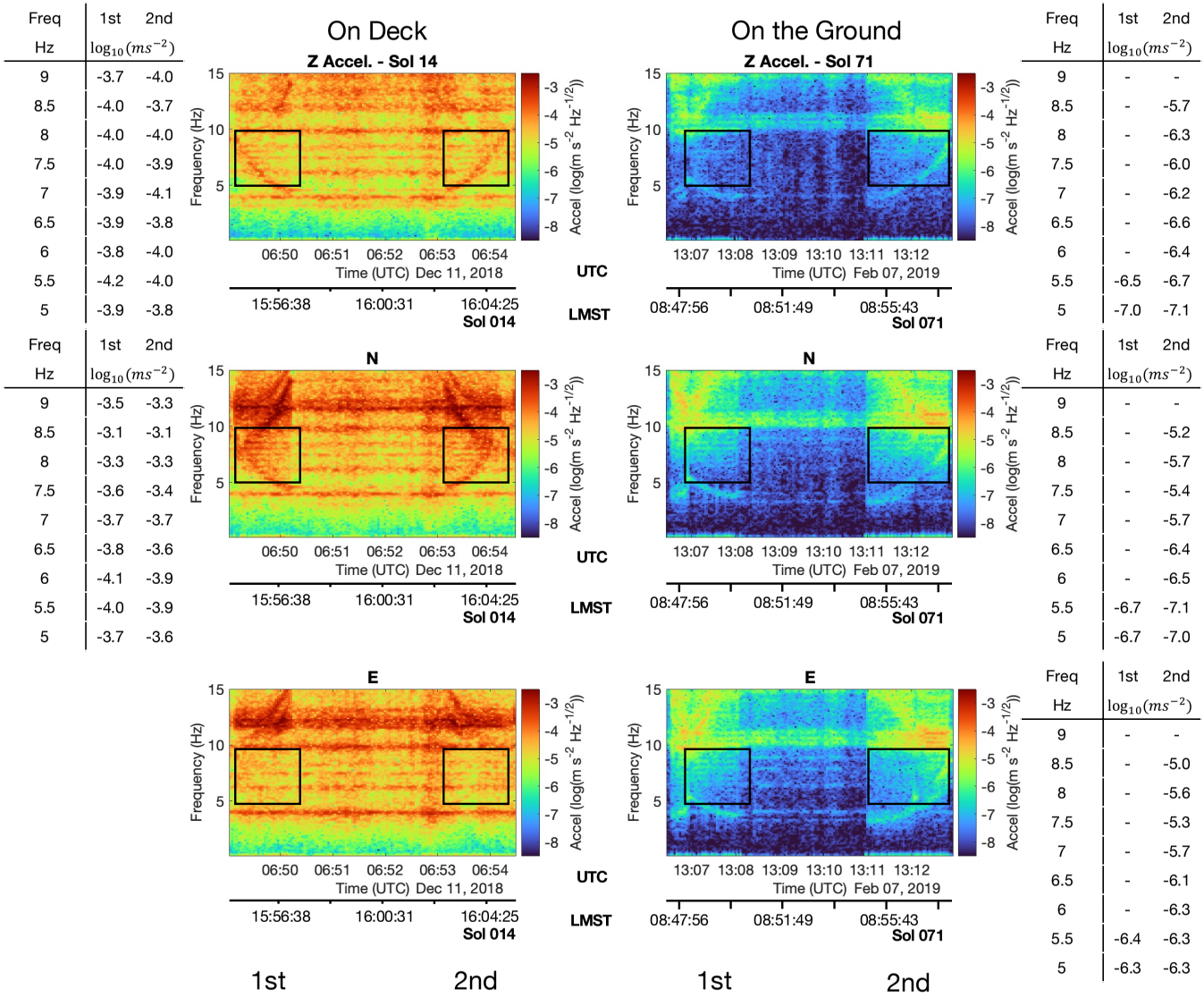

Freq Hz	1st $\log_{10}(ms^{-2})$	2nd $\log_{10}(ms^{-2})$
9	-3.7	-4.0
8.5	-4.0	-3.7
8	-4.0	-4.0
7.5	-4.0	-3.9
7	-3.9	-4.1
6.5	-3.9	-3.8
6	-3.8	-4.0
5.5	-4.2	-4.0
5	-3.9	-3.8

Freq Hz	1st $\log_{10}(ms^{-2})$	2nd $\log_{10}(ms^{-2})$
9	-3.5	-3.3
8.5	-3.1	-3.1
8	-3.3	-3.3
7.5	-3.6	-3.4
7	-3.7	-3.7
6.5	-3.8	-3.6
6	-4.1	-3.9
5.5	-4.0	-3.9
5	-3.7	-3.6

Freq Hz	1st $\log_{10}(ms^{-2})$	2nd $\log_{10}(ms^{-2})$
9	-	-
8.5	-	-5.7
8	-	-6.3
7.5	-	-6.0
7	-	-6.2
6.5	-	-6.6
6	-	-6.4
5.5	-6.5	-6.7
5	-7.0	-7.1

Freq Hz	1st $\log_{10}(ms^{-2})$	2nd $\log_{10}(ms^{-2})$
9	-	-
8.5	-	-5.2
8	-	-5.7
7.5	-	-5.4
7	-	-5.7
6.5	-	-6.4
6	-	-6.5
5.5	-6.7	-7.1
5	-6.7	-7.0

Freq Hz	1st $\log_{10}(ms^{-2})$	2nd $\log_{10}(ms^{-2})$
9	-	-
8.5	-	-5.0
8	-	-5.6
7.5	-	-5.3
7	-	-5.7
6.5	-	-6.1
6	-	-6.3
5.5	-6.4	-6.3
5	-6.3	-6.3

Figure 8. Determination of a transfer coefficient from robotic arm motions. The left of the middle two columns show the spectrogram of the two tau-pose robotic arm motions on and off the deck (Sol 14 and Sol 71) for the Z (vertical), N (north horizontal) and E (east horizontal) directions. Each has overlaid boxes highlighting the two chirp signatures per arm motion and the frequency range analysed. The outer columns are tables of the acceleration excited during each chirp motion for each frequency.

Figure 8 shows the spectrogram signatures for vertical (Z), north (N) and east (E) of the robotic arm for the similar, tau activity, arm motions on Sols 14 on the deck and 71 on the ground. The amplitude of the 4–9 Hz chirp signature is recorded in the tables either side of each component's spectrogram. This is done for both the first and second chirp in the motion. The excitations are taken from above 5 Hz as there is a known wind excited ambient mode at 4 Hz.

The mean value (taken from Figure 8) of excitation on the deck for the vertical and north components are $-3.9\log_{10}(\mathrm{m/s^2})$ and $-3.6\log_{10}(\mathrm{m/s^2})$ respectively while for on the ground they are $-6.5\log_{10}(\mathrm{m/s^2})$ and $-6.3\log_{10}(\mathrm{m/s^2})$. The uncertainty in each of these estimates of the mean is given by the confidence intervals, CI, as

$$CI = \frac{1.96\sigma}{(N)^{1/2}} \tag{3}$$

where 1.96 is a factor from the Student's t-distribution representing 95% confidence, σ is the standard deviation of the acceleration values and N is the number of values. A derivation of this confidence interval can be found in DeGroot et al. (2012).

The transfer coefficients are then given as -52±6 dB for the vertical and -54±10 dB for the north components, where the confidence interval is the sum of both the on and off deck confidence intervals for the mean acceleration value. An estimate for the east component is not given as the on deck signature of the robot arm motion does not have good enough SNR as only a portion can be seen above the noise in Figure 8.

Wind as a source of lander-induced noise

The wind is a major source of noise on Mars (Giardini et al., 2020; Lognonné et al., 2020; Murdoch et al., 2017). The sensitivity of the acceleration to wind has been examined through the notion of comodulation (Charalambous et al., 2020). This approach dictates that the acceleration signal power is correlated to the wind speed. To this end, the sensitivity of the SEIS-recorded signal to wind is determined by comparison of the root mean square (RMS) envelope of the acceleration signal to the wind speed. Calculating the RMS envelope for a specific bandwidth of acceleration allows the sensitivity to be examined over frequency.

Figure 9 shows the acceleration sensitivity obtained on the deck on Sol 21, on the ground prior to the WTS deployment on Sol 46 and in its final deployment covered by the WTS on Sol 268 for the

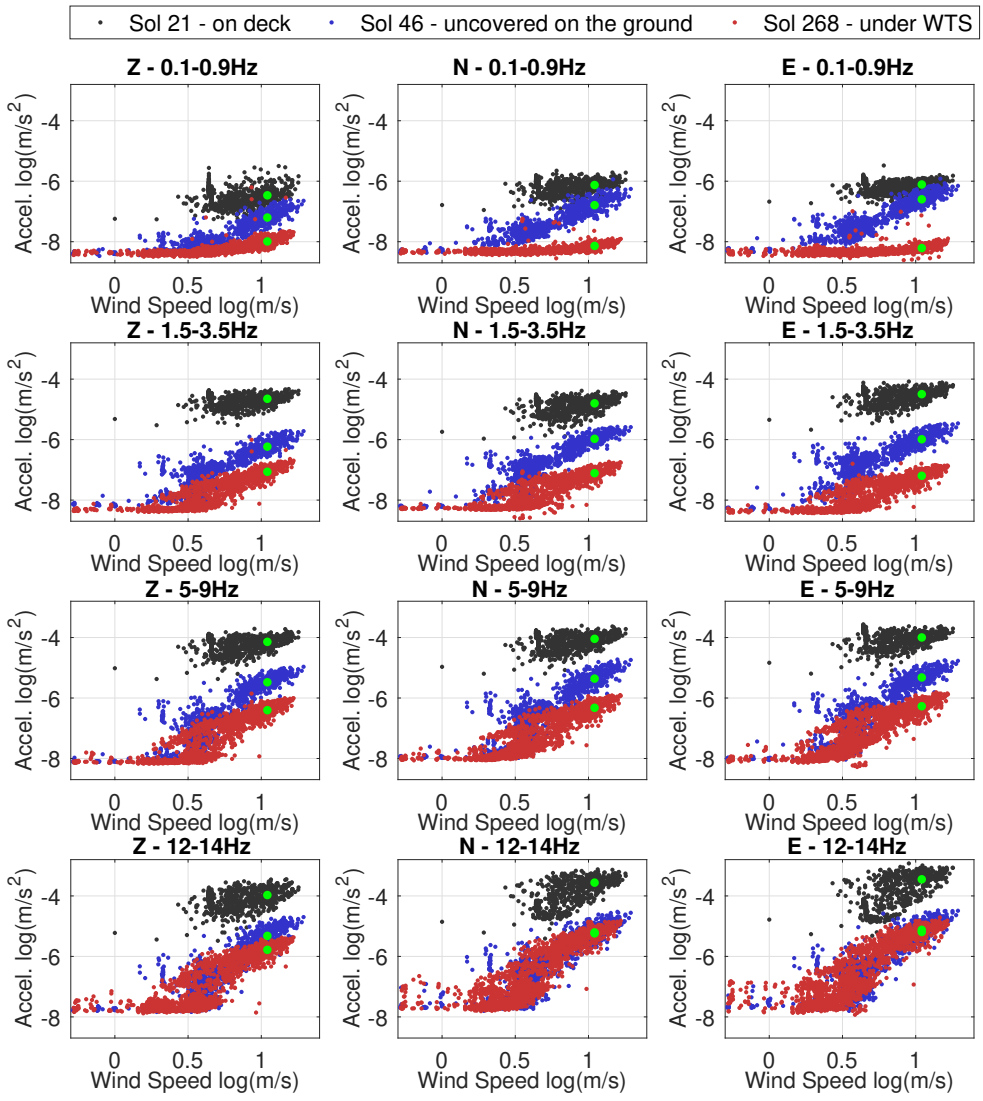

Figure 9. The wind speed versus RMS of the SP acceleration for Sol 21 on the deck (black), Sol 46 uncovered on the ground (blue) and Sol 268 under the WTS on the ground (red). This is shown for the Z (vertical), N (north horizontal) and E (east horizontal) components in the left to right columns. Each row demonstrates this sensitivity relationship for the acceleration in the bandwidths 0.1 – 0.9 Hz, 1.5 – 3.5 Hz, 5 – 9 Hz and 12 – 14 Hz from top to bottom. The green dots are the average acceleration at a wind speed of 11 m/s.

range of bandwidths: 0.1–0.9 Hz, 1.5–3.5 Hz, 5–9 Hz and 12–14 Hz. The 5–9 Hz bandwidth allows a direct comparison to the robot arm analysis. The 0.1–0.9 Hz bandwidth covers the majority of low

frequency marsquakes whereas the 1.5–3.5 Hz contains the 2.4 Hz resonance which is excited by higher frequency marsquakes (Clinton et al., 2021; Giardini et al., 2020). The 12–14 Hz bandwidth then gives a picture of higher frequencies. These bands also avoid the lander modes at 4 Hz and 10 Hz and tick noise at 1Hz (Ceylan et al., 2021).

The green dots on each curve in Figure 9 denote the mean RMS acceleration for a wind speed of 11 m/s, using the interval 10.5–11.5 m/s. This is done because the sensitivity to wind also depends on the current conditions, such as wind density and Reynolds number (Charalambous et al., 2020). Such wind speeds require similar strong turbulent conditions and so the acceleration values are comparable. These comparison of these values yields the signal amplitude attenuation between each deployment stage and are given in Table 4. These values then summarise the affect of placing SEIS on the ground and the emplacement of the WTS. Placing SEIS on the ground yields an attenuation of between -36±2 dB and -24±2 dB for frequencies above 1 Hz and between -14±2 dB and 10±2 dB below. For frequencies below 10 Hz, the WTS provides an attenuation of between -18±2 dB and -16±2 dB for the vertical component and -32±2 dB and -20±2 dB for the horizontal component. Above 10 Hz only the vertical component observes attenuation of -10±2 dB with none on the horizontals. This suggests that the direct influence of the wind on SEIS was much less important at these higher frequencies as there is little change before and after the direct forcing pathway on SEIS is removed by the WTS.

Bandwidth	Deck to ground, Sol 21 to 46 (dB)			WTS, Sol 46 to 268 (dB)		
	Z	N	E	Z	N	E
0.1–0.9 Hz	-14±2	-14±2	-10±2	-16±2	-26±2	-32±2
1.5–3.5 Hz	-32±2	-24±2	-30±2	-16±2	-22±2	-24±2
5–9 Hz	-26±2	-26±2	-26±2	-18±2	-20±2	-20±2
12–14 Hz	-26±2	-32±2	-34±2	-10±2	0±2	-2±2

Table 4: Summary of wind induced signal amplitude attenuation.

The full attenuation values between Sol 21 on the deck on Sol 268 are given in Table 5. This is the combination of the attenuation values provided by placing SEIS on the ground and then the WTS on top, that is, the total level of amplitude attenuation provided by the full deployment.

These total attenuation coefficients each have similar values for vertical and horizontal directions for the 1.5–3.5 Hz and 5–9 Hz bandwidths, aside from the east component in the 1.5–3.5 Hz band. At higher frequencies, in the 12–14 Hz range, the total attenuation is lower than the 1.5–9 Hz band indicating there is less apparent attenuation. For lower frequencies, in the 0.1–0.9 Hz band, the attenuation coefficients are also slightly lower than the 1.5–9 Hz range. In the 0.1–0.9 Hz band there is also a notable difference between the vertical and horizontal estimates, unlike all the values above 1 Hz, which are broadly equivalent in all axes aside from the east component in the 1.5–3.5 Hz bandwidth. If it is assumed that the wind generated seismic noise observed while covered on the ground is due to wind-induced lander vibrations, then these total attenuation coefficients represent transfer coefficient estimates. The validity of this assumption is discussed in the sequel.

Notice that on the deck the east component has a marginally higher sensitivity to wind than the north component in the 1.5–3.5 Hz bandwidth. The average RMS acceleration at 11 $\mathrm{m/s}$ wind speed is $3.2 \times 10^{-5}\,\mathrm{m/s^2}$ for the east component but $1.6 \times 10^{-5}\,\mathrm{m/s^2}$ for the north. This bears out in the east component total attenuation coefficient of -54±2 dB which is lower than the north component's -46±2 dB at 1.5–3.5 Hz. This feature may be caused by the lander geometry. Consider that the lander is aligned with the solar panels along the east/west axis but is due north of SEIS when it is on the ground. However, the distance between the lander and SEIS is not large compared to the distance between lander footpads. It should also be noted that there is a heterogeneity in at the InSight landing site (Garcia et al., 2020; Murdoch et al., 2020), whereby SEIS's location within the Homestead Hollow crater results in an increased compliance in the west direction.

Bandwidth	Robotic arm motions (dB)			Wind sensitivity changes (dB)		
	Z	N	E	Z	N	E
0.1–0.9 Hz				-30±2	-40±2	-42±2
1.5–3.5 Hz				-48±2	-46±2	-54±2
5–9 Hz	-52±6	-54±10		-46±2	-46±2	-46±2
12–14 Hz				-36±2	-34±2	-34±2

Table 5: Summary of transfer coefficient (signal amplitude attenuation from the lander deck to the ground) estimates.

Discussion and comparison of the observed transfer coefficients

The transfer/attenuation coefficients estimated from the robotic arm motions and the wind sensitivities are summarised in Table 5. These values are, in fact, summary statistics of the amplitude attenuation component of the transfer function between the lander deck and SEIS on the ground. To that end, it averages more complex aspects of the noise injection. For example, resonances, the response of the lander and the unloading of the deck (placement of instruments on the floor) may affect the comparison. Nevertheless, these values can be used to study the ambient noise injections at InSight. Here we will compare the values, assess their suitability as transfer coefficients and show what conclusions can be drawn about local noise sources of the InSight seismic station.

First consider the transfer coefficients estimated from the robotic arm motions. While the robot arm provides a useful known source of vibrations, it is not as suitable a source as the purpose built mechanical system used in the terrestrial studies of Teanby et al. (2017) and Myhill et al. (2018). For example, the SNR for the robotic arm signature in the east component is too low to accurately obtain a transfer coefficient estimate. It is also assumed that the robotic arm motions produce the same vibration by the lander each time. This is reasonable as the compared arm motions are very similar. Furthermore, it has been demonstrated that the compared chirp signals are only generated by the arm elbow position motor and not from ambient excitation, hence, the driving force is from the same mechanism. The confidence intervals do span a relatively wide range ($\pm$ 6 dB and $\pm$ 10dB) and so represent these limitations. This means that these transfer coefficients should be taken as a broad indication of the attenuation of lander generated signals.

Consider that the attenuation coefficients from the comparison of wind sensitivities on the deck and covered on the ground are indeed transfer coefficient estimates. In this case, the confidence intervals (all within $\pm$ 2 dB) suggest a relatively high level of statistical reliability compared to those from the robotic arm motion. This is because there are a larger amount of data points to compare. For these estimates to be interpreted as transfer coefficients, though, it must be assumed that the signal observed on the ground is due to wind-induced lander vibrations. Alternative pathways for wind-induced signals include wind-forcing on the WTS, HP3, nearby rocks or the ground itself. Should any of these dominate, then the combined attenuation value from the deck to the ground would not be appropriate to interpret as a transfer coefficient. Note that for these other forcing pathways, the wind speed obtained from TWINS is not the wind speed creating the force

as this, wind shear, scales with height (Murdoch et al., 2017). However, pre-mission modelling by Murdoch et al. (2017) and Mimoun et al. (2017) does indicate that wind-induced lander vibrations would be the dominant factor in these bandwidths. Furthermore, the attenuation given by the WTS deployment shown in Table 4 shows that it reduced the wind sensitivity for frequencies below $9\,\mathrm{Hz}$, removing the impact of direct forcing. The comparison of signals was also performed at a high wind speed of $11\,\mathrm{m/s}$ to ensure the atmospheric conditions (and so forcing) are comparable between the data sets.

Consider also that in the 5–$9\,\mathrm{Hz}$ band the attenuation coefficient estimated from the wind sensitivity is -46$\pm$2 dB for all components. This is within the range of the estimates from the robotic arm motions. Furthermore, the vertical and north component attenuation coefficient estimates in the 1.5–$3.5\,\mathrm{Hz}$ bandwidth are similar (-48$\pm$2 dB and -46$\pm$2 dB) to those in the 5–$9\,\mathrm{Hz}$ bandwidth. The east component has a lower value (-54$\pm$2 dB) than the 5–$9\,\mathrm{Hz}$ bandwidth which is explained by the east versus north wind sensitivity on the deck. All these values generally match the transfer coefficients estimated from the robotic arm motions. This further indicates that the combined attenuation coefficients could be interpreted as transfer coefficients as they generally match a value for a known signal from the lander. This, in turn, suggests that wind-induced lander vibrations are the dominant source of ambient seismic noise at the site in the 1.5–$9\,\mathrm{Hz}$ bandwidth. Outside of the 1.5–$9\,\mathrm{Hz}$ bandwidth the transfer coefficient estimates have different values. It is still possible, however, that the lander is responsible for wind driven background noise as the attenuation may change as a function of frequency.

A comparison between the observations and simple elastic models

The estimated transfer coefficients summarise the attenuation of the signal amplitude between the lander deck and SEIS's location on the ground. In this section we compare the InSight data to simple models of the regolith in order to highlight the various factors at play.

A key part of this attenuation is a geometric factor from the regolith, which is governed by its elastic properties. To a first approximation the regolith can be modelled as a homogeneous elastic half space. In this case the regolith is parameterised through an effective Young's modulus, Poisson's ratio and density throughout the medium, whereby its response to forcing/wave propagation

is provided by the elastic equations (Morgan et al., 2018). A value for such a model acts to average the parameters across the volume that the estimation method is sensitive to. At InSight such estimates have been obtained using pressure forcing (sensitive to tens of metres) through compliance by Garcia et al. (2020) and dust devils by Murdoch et al. (2020), which yielded a Young's modulus of 239 ± 140 MPa. The LVL resonances, on the other hand, gave a Young's modulus of 47 ± 10 MPa (Lognonné et al., 2020). This approach is sensitive to the top few centimetres and the measurement corresponds to the duricrust. The ground is equivalently paramaterised by p- and s- wave velocities. For example, Lognonné et al. (2020) use the Young's modulus estimate from the LVL resonances and assume a regolith density, ρ_r, of 1400 kg/m^3 to obtain an apparent p-wave velocity of 137 ± 15 m/s. The apparent p-wave velocity at a 1 metre scale was also directly measured from HP3 hammer strokes to be 118 ± 34 m/s. The difference/similarities in these results, which are sensitive to different scales, indicates that these properties do vary with depth. The local subsurface at InSight has been constrained using an inversion based on both pressure forcing and the HP3 hammering data which established parameter profiles down to 20 m (Kenda et al., 2020; Lognonné et al., 2020). This analysis considered a range of models including multiple layers, examining the effects of the regolith and bedrock.

An estimate of the effective Young's modulus from wind forcing on the lander

Consider the homogeneous elastic half space model for the regolith. We now estimate an effective Young's modulus for such a model by considering the ground response from wind forcing on the lander. From Teanby et al. (2017) the equation of motion for the lander and regolith response is given as

$$F = m\ddot{x} + \frac{6 r_f E}{1-\nu^2} x \tag{4}$$

where F is the vertical force applied to the lander, $m\ddot{x}$ is the inertial response of the lander (m is the mass of the lander and $\ddot{x}$ is the vertical acceleration of the lander) and $\frac{6 r_f E}{1-\nu^2} x$ is the is the approximate force from displacing the three lander feet by x, where r_f is the lander footpad radius, ν the Poisson's ratio and E the Young's modulus. A value of the force F applied to the lander can be obtained from the wind sensitivity. For a given wind speed a lift F_L and drag force F_D is applied to the lander as

$$F_L = \frac{1}{2} \rho_w C_L A_L u^2$$

$$F_D = \frac{1}{2}\rho_w C_D A_D u^2$$

where ρ_w is the wind density, C_L, C_D are the lift and drag coefficients, A_L, A_D is the surface area the wind is applied to and u is the wind speed. If we assume that the vertical acceleration, $\ddot{x}$, observed on the deck in Figure 9 is due to the lift force, F_L, and that the lander acts as a rigid body (so that the acceleration on the deck is that at the feet) then we can obtain an estimate of E from equation (4) where $F = F_L$. We take the confidence interval range around the average vertical acceleration in the 0.1–$0.9\,\mathrm{Hz}$ band at a wind speed of $11\,\mathrm{m/s}$ as in this band the lander is most likely to act as a rigid body. Using the required parameters, ρ_w, C_L, A_L, r_f and ν in Table 6 from Murdoch et al. (2017) we obtain the value $E = 62$–$81\,\mathrm{MPa}$. This estimate will have additional uncertainty based on the whether the prior assumptions/parameter values are appropriate. This value, however, is of a similar order to that obtained for a duricrust on the surface layer Lognonné et al. (2020) of $47 \pm 10\,\mathrm{MPa}$ and is lower than the estimates in Murdoch et al. (2020) of $239 \pm 140\,\mathrm{MPa}$. Our approach is sensitive to a shallower depth than that in Murdoch et al. (2020) as we examine local displacements. Kenda et al. (2020) find a similar Young's modulus at the surface, increasing with depth in a two-layer model.

Parameter	**Value**
g	$3.72\,\mathrm{m/s^2}$
r_f	$0.145\,\mathrm{m}$
C_L	0.1
A_L	$7.53\,\mathrm{m^2}$
ρ_w	$1.55 \times 10^{-2}\,\mathrm{kg/m^3}$
ρ_r in FEA	$1300\,\mathrm{kg/m^3}$
m	$365\,\mathrm{kg}$
ν	0.25
$\ddot{x}$ for 0.1–0.9 Hz	$3.0 \times 10^{-7}\,\mathrm{m/s^2}$ –$3.9 \times 10^{-7}\,\mathrm{m/s^2}$

Table 6: A table of parameter values used for Young's modulus estimation.

A comparison between the observations and simple elastic models

In this section, we compare the estimated transfer coefficients to a transfer coefficient derived from a simple elastic model of the regolith. The aim is to investigate the components which affect these transfer coefficients and provide context in terms of the regolith elastic behaviour. The pre-landing study of Teanby et al. (2017) examined analogue experiments in Iceland prior to launch to estimate the attenuation between the WTS and SEIS on the LVL. The WTS was replaced with a wind driven mass on a spring system (to provide a known source with good SNR) on a tripod surrounding an LVL model tripod both with disc feet to emulate the coupling. A follow-up study by Myhill et al. (2018) extended the analysis to a frequency band of 2–40 Hz, and conducted further experiments to study the attenuation at source-receiver distances up to 4 m. An analytical formula for the ratio of the vertical displacement at the LVL feet to the displacement of the WTS model feet, i.e. the vertical transfer coefficient, was derived for the case where the ground is a homogeneous elastic half space. Stott et al. (2020) implemented this formula for the case of the lander footpads to each SEIS foot yielding transfer coefficients of the order -19.2 dB. This value gives a much lower attenuation than any of our estimates in Table 5. A similar discrepancy between the experimental values and the analytical formula was also observed in the analogue experiments. Myhill et al. (2018) showed that the signal amplitude in the Icelandic analogue experiments decayed with distance r roughly as $A \sim r^{-n}$, with n$\sim$1.5–2.0, rather than n$\sim$1, as predicted for a homogeneous isotropic half-space. There are several possible causes of this more rapid attenuation. Regolith or lander anelasticity, depth-dependent elastic properties, or local increase in regolith Young's modulus beneath the lander/SEIS feet could all decrease effective transfer coefficients. Myhill et al. (2018) investigated one of these possibilities by implementing a finite element model (FEM) where the regolith is modelled as an elastic half space with a Poisson's ratio of 0.25 and a depth dependent Young's modulus. These models consider the static solution, neglecting inertial forces, and so are frequency independent. This is discussed in Myhill et al. (2018) who showed that it is appropriate for near-field displacements at these frequencies, whereas above 10 Hz inertial forces would need to be considered. Here we implement the same FEM adapted for the lander feet to SEIS interaction. To simulate the vertical and horizontal coupling between the lander footpads and the ground surface, we controlled the displacement of the surface along one Cartesian axis (i.e. motion along the E-, N- or Z-axis) underneath each footpad. On

other axes, and away from the footpads, the surface of the domain was allowed to deform freely. The Young's modulus profile is given by

$$E = E_0(b + z/r_f)^k \tag{5}$$

where the depth z is normalised by the lander footpad radius r_f, k determines the rate at which the Young's modulus increases with depth, E_0 is a reference Young's modulus and $b = \frac{\sigma_0}{\rho_r g r_f}$ is a dimensionless parameter dependent on the confining stress σ_0, the density ρ_r, the gravity g and the lander foot radius r_f. This formulation incorporates the depth variation of the Young's modulus observed in unconsolidated clays and sands due to the depth dependent increase in confinement pressure (Santamarina et al., 2001) and non-zero surface confining stress (Delage et al., 2017). The model is designed for small displacements of otherwise unstressed regolith, and so does not include the stresses on the regolith deriving from the weights of the lander or SEIS. The displacement ratio map around the lander for $k = 0.9$ and $b = 10$ or 1 is shown in Figure 10 for motions in each of the three axes.

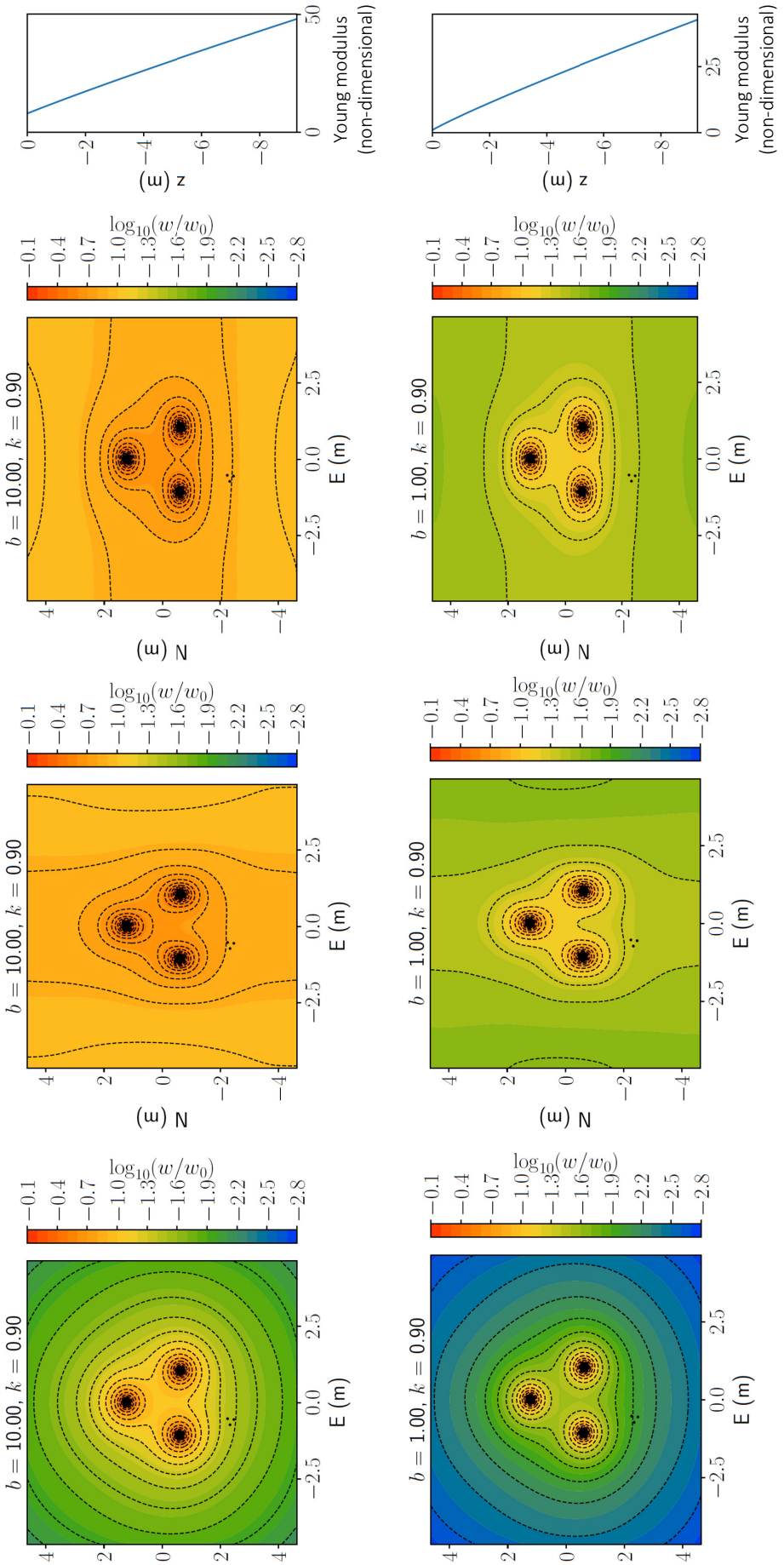

Figure 10. The relative displacement, w, observed around InSight for a given displacement of the lander feet, w_0, predicted by the elastic model (5). From left to right: vertical displacement, north-south displacement, and east-west displacement. The large black circles correspond to the positions of the lander feet. The small black circles correspond to the positions of the SEIS feet.

Figure 11 shows the relative vertical, north-south and east/west displacement ratios (transfer coefficients) predicted by the FEM at each SEIS foot for vertical, north/south and east/west motions respectively over a range of k and b. The transfer coefficient of ∼-49 dB estimated for the 1.5–$9\,\mathrm{Hz}$ bandwidth requires a high value of $k =\sim 0.9$ and a low value of $b =\sim 0.01$ to explain the observed attenuation as from the propagation in the regolith. The value of k in the model (5) is linked to the amplitude decay with distance $A \sim r^{-n}$ by $n = 1 + k$. The value of $k = 0.9$ gives a decay proportional to $n = -1.9$, which is close to that measured at Fellabær by Myhill et al. (2018). The value of b is related to the effective confining stress over the surface between the lander and SEIS and is homogeneous in this model. The confining stress is given as $\sigma_0 = F/A$ where F is a force on the surface over an area, A. Consider that the lander will have a significant effect nearby. If it is assumed that the weight of the lander dominates then the force is due to the weight of the lander, $F = mg$ spread over the three lander footpads as $A = 3\pi r_f^2$. Using the values in Table 6 gives $\sigma_0 = 6840\,\mathrm{Pa}$ which leads to an expected value of $b = 9.77$ using the regolith density of $\rho_r = 1300\,\mathrm{kg/m^3}$ from Delage et al. (2017). This value is much greater than the $b =\sim 0.01$ required to describe the 1.5–$9\,\mathrm{Hz}$ bandwidth. This can be interpreted as the effect of the lander on the confining stress being localised to the area underneath the lander feet, or to a strong variation in density. Another potentially significant factor is that the lander may not act as a rigid body in this frequency range. As a result, the acceleration obtained on the deck does not correspond to that at the feet, that is, the lander legs attenuate some of the deformation experienced by the lander deck.

Consider now the transfer coefficient estimates in the 0.1–$0.9\,\mathrm{Hz}$ bandwidth estimated from the wind sensitivity changes in Figure 9. The vertical transfer coefficient is -30±2 dB shows less attenuation than the horizontals which are -40±2 dB and -42±2 dB. In this frequency band the lander may act more as a rigid body, as indicated by the reduced attenuation. The vertical component could be matched by a set of parameters k =0.7–0.9 and b =1–5, through consideration of Figure 11. However, both vertical and horizontal transfer coefficients cannot be produced using the model (5) by any value of k and b as the horizontal attenuation is less than or similar to the vertical.

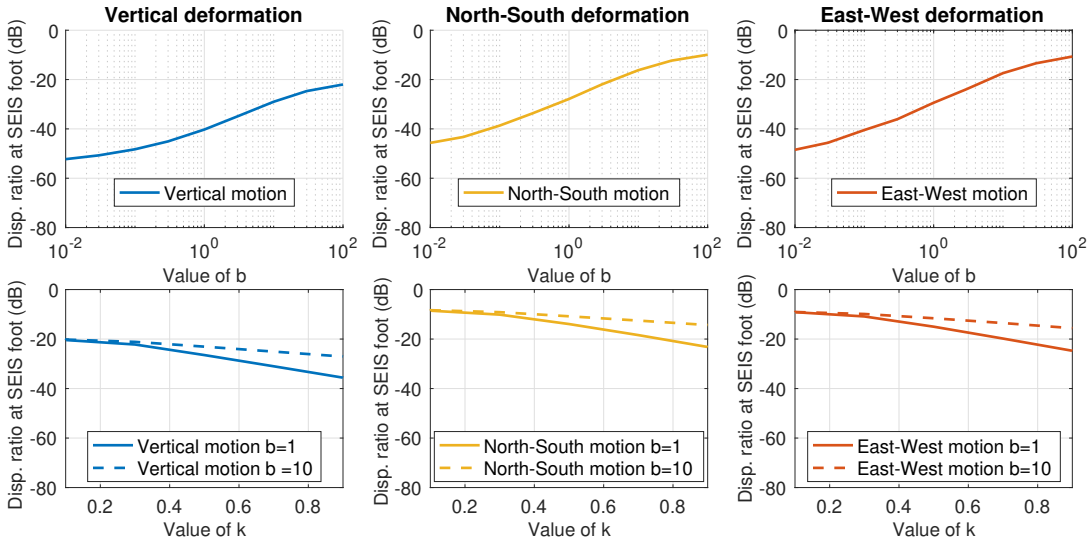

Figure 11. Average displacement of the three SEIS feet as a ratio of the lander feet displacement (the transfer coefficient) from the FEA where the Young's modulus is given by $E = E_0(b + z/r_f)^k$ (5) over different k and b parameters where k corresponds to the depth variation and b is linked to the surface confining stress. Each column shows the displacement amplitude attenuation for vertical, north-south and east-west deformations from left to right. The attenuation for the vertical deformation is the corresponding vertical motion of the lander and the horizontal motions are the respective in-plane motion to the deformation. The top row gives the transfer coefficient for a fixed $k = 0.9$ over a range of values of b and the bottom row shows the transfer coefficient for the fixed values of $b = 1$ and $b = 10$ over a range of k.

Conclusion

Two algorithms were proposed to derive the tilt from the SP mass position data. The first of these took the mass position value of both the horizontal SP sensors when SP2 reached a reference temperature. The second algorithm removed the fitted thermal response model proposed in Stott et al. (2018a) for each sensor. These algorithms calculate the tilt on a Sol to Sol basis and so provide an estimate of the relative, delta tilt. This makes them reasonably robust to data gaps/outlying data.

The two tilt extraction algorithms were applied to the deployment data, from when SEIS was on the deck to when it was fully covered by the WTS on the ground. The tilt estimates over this period show the overall settling of the sensor after site modifications such as levelling and

the effect of actions including the TSB release, LSA release, pinning mass adjustments and WTS deployment itself. The tilt estimation algorithms were then applied over 667 Sols (one Martian year) of data throughout the science monitoring phase. This showed that the SEIS assembly has remained extremely stable to a change in tilt of $<$0.007 degrees throughout.

The SP data from deployment is also useful to examine the local noise sources at InSight. To do so, we compared the acceleration observed by the SP seismometer on and off the deck. Vibrations from robotic arm motions are found to be attenuated by -52$\pm$6 dB and -54$\pm$10 dB for the vertical and north components respectively. These values are estimates of the amplitude attenuation of lander generated signals to SEIS, that is, the transfer coefficient.

The wind induced vibrations are decomposed for attenuation between moving SEIS to the ground and then by the WTS. For frequencies above 1 Hz, moving SEIS to the ground from the deck reduces wind induced signals by $\sim$-28 dB. Below 1 Hz the attenuation is slightly lower at $\sim$-12 dB. For frequencies below 10 Hz, the emplacement of the WTS attenuates wind induced vibrations by $\sim$-16 dB for vertical and $\sim$-25 dB for horizontal components. Above 10 Hz, the WTS only has an effect on the vertical component with an attenuation of -10$\pm$2 dB. This means that the horizontal components may not have been affected by direct wind forcing on SEIS at these frequencies before the WTS was deployed. Wind induced vibrations under the WTS on the ground are $\sim$-49 dB lower than on the deck in the 1.5–3.5 Hz and 5–9 Hz bandwidths. These total attenuation values are of a similar order to the robot arm estimates, a known source from the lander. This suggests they are also estimates of the transfer coefficient and that wind induced lander vibrations are the dominant source of ambient noise, as expected in the pre-landing studies of Mimoun et al. (2017); Murdoch et al. (2017). Below 1 Hz, the full attenuation is by $\sim$-30 dB and $\sim$-41 dB for the vertical and horizontal components respectively. Above 10 Hz, the full attenuation is by $\sim$-35 dB for each component. The background wind noise could also be generated by the lander in these bandwidths as frequency dependent factors may play a part.

The transfer coefficients provide a broad indication of the attenuation between the lander deck and SEIS on the ground. An FEM was implemented to explore the contribution of geometric attenuation in the regolith. To explain the observed attenuation of $\sim$-49 dB, a fast Young's modulus increase with depth is required, of a similar value to those seen in terrestrial studies. However, the parameter describing the surface confining stress is required to be a factor of $\sim$100 lower than

that for a calculation for directly under the lander feet. The FEM also cannot explain the change in attenuation with frequency observed in the wind induced signal attenuation values, should they be taken as transfer coefficient estimates. Several other factors not considered by the FEM may contribute to the transfer coefficient estimates. These include: attenuation from the lander legs, local ground discontinuities, the inertial response of the regolith, elastic anisotropy and anelasticity.

Considering the regolith as a homogeneous elastic half space, the effective Young's modulus is estimated to be $E = 62$–$81\,\mathrm{MPa}$ based on the vertical acceleration below $1\,\mathrm{Hz}$, the equation of motion for the lander and the candidate wind forcing. This value is close to the duricrust estimate of $47 \pm 10\,\mathrm{MPa}$ (Lognonné et al., 2020) and lower than the pressure forcing estimates of $239 \pm 140\,\mathrm{MPa}$ (Murdoch et al., 2020). Our approach is sensitive to a shallower depth than the pressure forcing estimates and so this can be reconciled.

This work uses the data from SP sensor during the deployment phase of the InSight Mission to provide data-centric context for the SEIS experiment's observations. The tilt estimates are useful to examine long period variation at InSight and also provide a story of the SEIS deployment. The tilt algorithms are designed for high noise environments, where temperature is the dominant factor. Future developments could incorporate other factors such as pressure. The transfer coefficient estimates are important to understand the noise injection at InSight. They can be incorporated into the mission noise models of Mimoun et al. (2017); Murdoch et al. (2017) and used to update the forward model for decorrelation attempts such as in Hurley et al. (2018). The lack of anthropogenic/cultural sources or an ocean microseism mean that the the affect of wind in seismic data can be better isolated on Mars in comparison to Earth data, where it is also a concern. For example, Dybing et al. (2019) observed similar a relationship to wind. The field of planetary seismology is set to grow with seismometers planned on missions to the Moon (Nunn et al., 2021) and Titan (Lorenz et al., 2019) along with further concepts for ocean worlds (Vance et al., 2021). To that end, this study yields information about operating a seismometer on Mars both on a lander deck and on the surface. The approaches used could also be extended for terrestrial data, in particular for lesser isolated stations.

Data and Resources

The InSight SEIS (seismic sensor) and TWINS (wind speed) data used in this paper are available from the IPGP Datacenter and IRIS-DMC (InSight Mars SEIS Data Service, 2019b) and are also available from the NASA PDS (National Aeronautics and Space Administration Planetary Data System, https://pds.nasa.gov/, (InSight Mars SEIS Data Service, 2019a)).

The finite element model was adapted from (Myhill et al., 2018) using the FEniCS Project Python package (Alnæs et al., 2015; Logg et al., 2012). The code will be made available on Github.

Acknowledgements

This paper is InSight contribution number 205. We acknowledge NASA, CNES, their partner agencies and institutions (UKSA, SSO, DLR, JPL, IPGP-CNRS, ETHZ, IC, MPS-MPG) and the flight operations team at JPL, SISMOC, MSDS, IRIS-DMC and PDS for providing SEED SEIS data. This work was supported in part by funding from the UK space agency the French Space Agency CNES and ANR (ANR-19-CE31-0008-08). The authors would like to thank Victor Tsai as the editor, Adam Ringler and an anonymous reviewer for their comments.

References

Alnæs, M., J. Blechta, J. Hake, A. Johansson, B. Kehlet, A. Logg, C. Richardson, J. Ring, M. E. Rognes, and G. N. Wells (2015). The FEniCS project version 1.5, Archive of Numerical Software, 3(100).

Banerdt, W. B., S. E. Smrekar, D. Banfield, D. Giardini, M. Golombek, C. L. Johnson, P. Lognonné, A. Spiga, T. Spohn, C. Perrin, et al. (2020). Initial results from the InSight mission on Mars, Nat. Geosci., 13(3) 183-189.

Banfield, D., A. Spiga, C. Newman, F. Forget, M. Lemmon, R. Lorenz, N. Murdoch, D. Viudez-Moreiras, J. Pla-Garcia, R. F. Garcia, et al. (2020). The atmosphere of Mars as observed by InSight, Nat. Geosci., 13(3) 190-198.

724 Bierwirth, M., A. Kramer, M. Eberhardt, and F. IJpelaan (2019). Leveling the SEIS instrument
725 on NASA's InSight mission to Mars, Proceedings of the European Space Mechanisms and
726 Tribology Symposium

727 Ceylan, S., J. F. Clinton, D. Giardini, M. Böse, C. Charalambous, M. van Driel, A. Horleston,
728 T. Kawamura, A., Khan, G. Orhand-Mainsant, J.-R. Scholz, S. C. Stähler, F. Euchner, W. B.
729 Banerdt, P. Lognonné, D. Banfield, E. Beucler, R. F. Garcia, S. Kedar, M. Panning, W. T. Pike,
730 S. E. Smrekar, A. Spiga, N. L. Dahmen, K. Hurst, A. E. Stott, R. D. Lorenz, M. Schimmel, E.
731 Stutzmann, J. ten Pierick, V. Conejero, C. Pardo, and C. Perrin (2021). Companion guide to the
732 Marsquake Catalog from InSight, Sols 0-478: data content and non-seismic events, Phys. Earth
733 Planet. In., 310 106597.

734 Charalambous, C., A. E. Stott, W. T Pike, J. McClean, T. Warren, A. Spiga, D. Banfield, D.,
735 R. F. Garcia, J. Clinton, S. C. Stähler, et al. (2020). A comodulation analysis of atmospheric
736 energy injection into the ground motion at insight, Mars, J. Geophys. Res.: Planets, 126
737 e2020JE006538.

738 Clinton, J. F., S. Ceylan, M. van Driel, D. Giardini, S. C. Stähler, M. Böse, C. Charalambous, N. L.
739 Dahmen, A. Horleston, T. Kawamura, A. Khan, G. Orhand-Mainsant, J.-R. Scholz, F. Euchner,
740 W. B. Banerdt, P. Lognonné, D. Banfield, E. Beucler, S. Kedar, M. Panning, C. Perrin, W. T.
741 Pike, S. E. Smrekar, A. Spiga, and A. E. Stott (2021). The Marsquake Catalogue from InSight,
742 Sols 0-478, Phys. Earth Planet. In., 310 106595

743 De Angelis, S. and P. Bodin (2012). Watching the wind: Seismic data contamination at long periods
744 due to atmospheric pressure-field-induced tilting, Bull. Seism. Soc. Am., 102(3) 1255–1265.

745 DeGroot, M. H. and M. J. Schervish (2012). Probability and statistics, Pearson Education.

746 Delage, P., F. Karakostas, A. Dhemaied, M. Belmokhtar, P. Lognonné, M. Golombek, E. De Laure,
747 K. Hurst, J.-C. Dupla, S. Kedar, Sharon, et al. (2017). An investigation of the mechanical
748 properties of some Martian regolith simulants with respect to the surface properties at the InSight
749 mission landing site, Space. Sci. Rev., 211(1-4) 191–213.

Dybing, S. N., A. T. Ringler, D. C. Wilson, and R. E. Anthony (2019). Characteristics and Spatial Variability of Wind Noise on Near-Surface Broadband Seismometers, Bull. Seism. Soc. Am., 109(3) 1082–1098.

Garcia, R. F., B. Kenda, T. Kawamura, A. Spiga, N. Murdoch, P. Lognonné, R. Widmer-Schnidrig, N. Compaire, G. Orhand-Mainsant, D. Banfield, et al. (2020). Pressure Effects on the SEIS-InSight Instrument, Improvement of Seismic Records, and Characterization of Long Period Atmospheric Waves From Ground Displacements, J. Geophys. Res.: Planets, 125(7) e2019JE006278.

Giardini, D., P. Lognonné, W. B. Banerdt, W. T. Pike, U. Christensen, S. Ceylan, J. F. Clinton, M. van Driel, S. C. Stähler, M. Böse, et al. (2020). The seismicity of Mars, Nat. Geosci., 13(3) 205–212.

Golombek, M., D. Kipp, N. Warner, I. Daubar, R. Fergason, R. L. Kirk, R. Beyer, A. Huertas, S. Piqueux, N. E. Putzig, et al. (2017). Selection of the InSight landing site, Space. Sci. Rev., 211(1) 5–95.

Hurley, J., N. Murdoch, N. A. Teanby, N. Bowles, T. Warren, S. B. Calcutt, D. Mimoun, and W. T. Pike (2018). Isolation of Seismic Signal from InSight/SEIS-SP Microseismometer Measurements, Space. Sci. Rev., 214(5) 95.

InSight Mars SEIS Data Service (2019a). InSight SEIS Data Bundle. PDS Geosciences (GEO) Node, https://doi.org/10.17189/1517570.

InSight Mars SEIS Data Service (2019b). SEIS raw data, Insight Mission. IPGP, JPL, CNES, ETHZ, ICL, MPS, ISAE-Supaero, LPG, MFSC, https://doi.org/10.18715/SEIS.INSIGHT.XB_2016.

Kenda, B., M. Drilleau, R. F. Garcia, T. Kawamura, N. Murdoch, N. Compaire, P. Lognonné, A. Spiga, R. Widmer-Schnidrig, P. Delage, et al. (2020). Subsurface structure at the InSight landing site from compliance measurements by seismic and meteorological experiments, J. Geophys. Res.: Planets, 125(6) e2020JE006387.

776 Kümpel, H.-J., K. Lehmann, M. Fabian, and G. Mentes (2001). Point stability at shallow depths:
777 experience from tilt measurements in the Lower Rhine Embayment, Germany, and implications
778 for high-resolution GPS and gravity recordings, Geophys. J. Int., 146(3) 699–713.

779 Liu, H., W. T. Pike, C. Charalambous and A. E. Stott (2019). Passive Method for Reducing Tem-
780 perature Sensitivity of a Microelectromechanical Seismic Accelerometer for Marsquake Moni-
781 toring Below 1 Nano-g, Physical Review Applied, 12(6) 064057.

782 Logg, A., K.-A. Mardal, and G. N. Wells (2012). Automated solution of differential equations by
783 the finite element method: The FEniCS book, Springer Science & Business Media.

784 Lognonné, P., W. B. Banerdt, D. Giardini, W. T. Pike, U. Christensen, P. Laudet, S. De Raucourt, P.
785 Zweifel, S. Calcutt, M. Bierwirth, et al. (2019). SEIS: Insight's seismic experiment for internal
786 structure of Mars, Space. Sci. Rev., 215(1):12.

787 Lognonné, P., W. B. Banerdt, W. T. Pike, D. Giardini, U. Christensen, R. F. Garcia, T. Kawamura,
788 S. Kedar, B. Knapmeyer-Endrun, B., L. Margerin, F. Nimmo, M. Panning, B. Tauzin, J.-R.
789 Scholz, et al. (2020). Constraints on the shallow elastic and anelastic structure of Mars from
790 InSight seismic data, Nat. Geosci..13(3): 213-220.

791 Lorenz, R. D., M. Panning, S. C. Stähler, H. Shiraishi, R. Yamada, and E. P. Turtle (2019). Titan
792 Seismology with Dragonfly: Probing the Internal Structure of the Most Accessible Ocean World,
793 51st Lunar and Planetary Science Conference.

794 Maki, J. N., M. Golombek, R. Deen, H. Abarca, C. Sorice, T. Goodsall, M. Schwochert, M. Lem-
795 mon, A. Trebi-Ollennu, and W. B. Banerdt (2018). The color cameras on the InSight lander,
796 Space. Sci. Rev., 214(6) 105.

797 McClean, J. B., W. T. Pike, C. Charalambous, A. E. Stott, T. Warren, S. Calcutt, I. M. Standley, P.
798 Lognonné, and W. B. Banerdt (2019). Operation of the InSight Short Period (SP) Seismometers
799 During Cruise, 51st Lunar and Planetary Science Conference.

800 Mimoun, D., N. Murdoch, P. Lognonné, K. Hurst, W. T. Pike, J. Hurley, T. Nébut, W. B. Banerdt,
801 et al. (2017). The noise model of the SEIS seismometer of the InSight mission to Mars, Space.
802 Sci. Rev., 211(1-4) 383–428.

803 Morgan, P., M. Grott, B. Knapmeyer-Endrun, M. Golombek, P. Delage, P. Lognonné, S. Piqueux,
804 I. Daubar, N. Murdoch, C. Charalambous, et al. (2018). A pre-landing assessment of regolith
805 properties at the InSight landing site, Space. Sci. Rev., 214(6) 104.

806 Murdoch, N., D. Alazard, B. Knapmeyer-Endrun, N. Teanby, and R. Myhill (2018). Flexible mode
807 modelling of the InSight lander and consequences for the SEIS instrument, Space. Sci. Rev.,
808 214(8) 117.

809 Murdoch, N., D. Mimoun, R. F. Garcia, W. Rapin, T. Kawamura, P. Lognonné, D. Banfield, and W.
810 B. Banerdt (2017). Evaluating the Wind-Induced Mechanical Noise on the InSight Seismome-
811 ters, Space. Sci. Rev., 211(1) 429–455.

812 Murdoch, N., A. Spiga, R. D. Lorenz, R. F. Garcia, C. Perrin, R. Widmer-Schnidrig, S. Rodriguez,
813 N. Compaire, N. H. Warner, D. Mimoun, D. Banfield, P. Lognonné, and W. B. Banerdt (2020).
814 Constraining Martian regolith parameters and vortex trajectories from combined seismic and
815 meteorological measurements, J. Geophys. Res.: Planets, 126(2) e2020JE006410.

816 Myhill, R., N. Teanby, J. Wookey, and N. Murdoch (2018). Near-field seismic propagation and
817 coupling through Mars' regolith: implications for the InSight Mission, Space. Sci. Rev., 214(5)
818 85.

819 Nunn, C., W. T. Pike, I. M. Standley, S. Calcutt, S. Kedar, and M. Panning (2021). Standing on
820 Apollo's Shoulders: a Microseismometer for the Moon, The Planetary Science Journal, 2(1)
821 36.

822 Panning, M. P., W. T. Pike, P. Lognonné, W. B. Banerdt, N. Murdoch, D. Banfield, C. Charalam-
823 bous, S. Kedar, R. D. Lorenz, A. G. Marusiak, J. B. McClean, C. Nunn, S. C. Stähler, A. E.
824 Stott, and T. Warren (2020). On-Deck Seismology: Lessons from InSight for Future Planetary
825 Seismology, J. Geophys. Res.: Planets, 125(4) 1–13.

826 Petrosino, S., C. Ricco, E. De Lauro, I. Aquino, and M. Falanga (2020). Time evolution of medium
827 and long-period ground tilting at Campi Flegrei caldera, ADGEO, 52 9–17.

828 Pike, W. T., S. Calcutt, I. M. Standley, A. G. Mukherjee, J. Temple, T. Warren, C. Charalambous,

H. Liu, A. E. Stott, and J. B. McClean (2016). A silicon seismic package (SSP) for planetary geophysics, 47th Lunar and Planetary Science Conference.

Ringler, A. T., J. Steim, D. C. Wilson, R. Widmer-Schnidrig, and R. E. Anthony (2020). Improvements in seismic resolution and current limitations in the Global Seismographic Network, Geophys. J. Int., 220(1) 508–521.

Rodgers, P. W. (1968). The response of the horizontal pendulum seismometer to Rayleigh and Love waves, tilt, and free oscillations of the Earth. Bull. Seism. Soc. Am., 58(5) 1385–1406.

Santamarina, J. C., K. A. Klein, and M. A. Fam (2001). Soils and waves, J. Wiley & Sons New York.

Sorrells, G. G. (1971). A preliminary investigation into the relationship between long-period seismic noise and local fluctuations in the atmospheric pressure field. Geophys. J. Int., 26(1-4) 71–82.

Stott, A. E., C. Charalambous, J. B. McClean, T. Warren, A. Trebi-Ollennu, G. Lim, N. A. Teanby, R. Myhill, A. Horleston, S. Kedar, et al. (2020). Using InSight's Robotic Arm Motion to Examine the Martian Regolith's Response to Short Period Vibrations, 51st Lunar and Planetary Science Conference.

Stott, A. E., C. Charalambous, T. Warren and W. T. Pike (2018). Full-band signal extraction from sensors in extreme environments: the NASA InSight microseismometer, IEEE Sensor J., 18(22) 9382–9392.

Stott, A. E. (2018). Latent variable regression and applications to planetary seismic instrumentation, Imperial College London Thesis.

Teanby, N. A., J. Stevanović, J. Wookey, N. Murdoch, J. Hurley, R. Myhill, N. Bowles, S. Calcutt, and W. T. Pike (2017). Seismic coupling of short-period wind noise through Mars' regolith for NASA's InSight lander, Space. Sci. Rev., 211(1-4) 485–500.

Trebi-Ollennu, A., W. Kim, K. Ali, O. Khan, C. Sorice, P. Bailey, J. Umland, et al. (2018). InSight Mars Lander Robotics Instrument Deployment System, Space. Sci. Rev., 214(5) 93.

855 Vance, S., M. Behounkova, B. G. Bills, P. Byrne, O. Cadek, J. Castillo-Rogez, G. Choblet, K.
856 Hughson, S. Hurford, J. Keane, et al. (2021). Distributed Geophysical Exploration of Enceladus
857 and Other Ocean Worlds, Bull. Am. Astron. Soc., 53(4) 127.

858 Wielandt, E., and G. Streckeisen (1982). The leaf-spring seismometer: Design and performance,
859 Bull. Seism. Soc. Am., 72(6A) 2349–2367.

860 Wolin, E., S. van der Lee, T. A. Bollmann, D. A. Wiens, J. Revenaugh, F. A. Darbyshire, A. W.
861 Frederiksen, S. Stein, and M. E. Wysession (2015). Seasonal and diurnal variations in long-
862 period noise at SPREE stations: The influence of soil characteristics on shallow stations' per-
863 formance, Bull. Seism. Soc. Am., 105(5) 2433–2452.